Spread of pathological human Tau from neurons to oligodendrocytes and loss of high-firing pyramidal neurons in ageing mice

Tim J. Viney[1]*, Barbara Sarkany[1], A. Tugrul Ozdemir[1], Katja Hartwich[1,2], Judith Schweimer[1,3], David Bannerman[4], Peter Somogyi[1].

[1]Department of Pharmacology, University of Oxford, Oxford, OX1 3QT ,UK.

[2]Current address: Medical Research Council Brain Network Dynamics Unit, Nuffield Department of Clinical Neurosciences, University of Oxford, Oxford, OX3 7BN, UK.

[3]Current address: Boehringer Ingelheim Pharma GmbH & Co. KG, Biberach, 88397, Germany.

[4]Department of Experimental Psychology, University of Oxford, Oxford, OX2 6GG, UK.

*Lead Contact. Correspondence: tim.viney@pharm.ox.ac.uk (T.J.V.)

Abstract

Intracellular aggregation of hyperphosphorylated Tau (pTau) in the brain is associated with cognitive and motor impairments, and ultimately neurodegeneration. We investigate how human pTau affects cells and network activity in the hippocampal formation of THY-Tau22 tauopathy model mice *in vivo*. We find that pTau preferentially accumulates in deep-layer pyramidal neurons, leading to neurodegeneration, and we establish that pTau spreads to oligodendrocytes. During goal-directed virtual navigation in aged transgenic mice, we detect fewer high-firing prosubicular pyramidal cells but the firing population retains its coupling to theta oscillations. Analysis of network oscillations and firing patterns of pyramidal and GABAergic neurons recorded in head-fixed and freely-moving mice suggests preserved neuronal coordination. In spatial memory tests, transgenic mice have reduced short-term familiarity but spatial working and reference memory are surprisingly normal. We hypothesize that unimpaired subcortical network mechanisms maintain cortical neuronal coordination, counteracting the widespread pTau aggregation, loss of high-firing cells, and neurodegeneration.

Introduction

The majority of tauopathies, defined by intracellular accumulation of hyperphosphorylated Tau proteins (pTau), are 'sporadic', and a minority are inherited, caused by mutations of the microtubule-associated protein Tau (*MAPT*) gene.[1] Humans express six isoforms in the brain, with 3 containing three repeats (3R) each and 3 others containing four repeats (4R) each arising from splice variants.[1] These isoforms accumulate in different kinds of neurons and glia in different tauopathies, and can have different spatiotemporal distributions. Alzheimer's disease, amyotrophic lateral sclerosis, Niemann-Pick disease type C and some types of familial frontotemporal dementia and parkinsonism (FTDP) have a mixture of 3R and 4R Tau. Those with only 3R Tau include Pick's disease and some types of FTDP. The 4R tauopathies include corticobasal degeneration (CBD), progressive supranuclear palsy (PSP), argyrophilic grain disease, and other types of FTDP.[1,2] The impact on cognitive and motor functions depend on which brain regions and cell types are most vulnerable to developing pTau aggregates and the extent of neurodegeneration. Deficits in spatial memory – our ability to

encode and recall environmental contexts – are strongly associated with cortical pTau-related progression from mild cognitive impairment to Alzheimer's disease.[3-5] It is generally accepted that the spread of pTau correlates with severity of neurological symptoms, with age being the greatest risk factor.

Animal models provide a wealth of information about the impact of pTau on various aspects of behavior, cognition, network excitability, and plasticity. Tauopathy models can suffer from progressive motor impairments,[6-8] making it difficult to perform investigations using physiologically-relevant aged animals. We therefore investigated how aggregation of mutant human 4R Tau affected spatial memory and neuronal coordination in awake behaving mice at different ages using the well-characterized THY-Tau22 mouse line. This line gradually develops pTau inclusions from 2-3 months of age,[9] and has a less severe phenotype than related lines,[8,10] ideal for investigating cumulative effects of pTau in aged mice. Importantly, heterozygous transgenic (tg) mice and their non-transgenic (ntg) littermates do not develop significant motor impairments during ageing, enabling behavioral testing and awake *in vivo* electrophysiological recordings. Tg mice display prominent neurofibrillary tangles (accumulation of human pTau in somata) as well as neuropil threads (pTau in other processes such as axons). We found that ageing tg mice – which had normal life expectancy – had hippocampal neurodegeneration, showed a reduction in high firing pyramidal neurons, and exhibited reduced short-term familiarity for spatial cues, with pTau spreading from neurons to oligodendrocytes. Despite these changes, neuronal coupling to theta oscillations, and spatial working and reference memory performance showed no detectable differences. We hypothesize that this is due to unimpaired network mechanisms that govern cortical neuronal coordination.

Results

Distribution of pTau in ageing mice

To understand how pTau aggregation affects neuronal and network activity, we first mapped pTau in brains of tg mice at different ages. By 2-3 months old (mo), clusters of AT8 immunoreactive (pTau+) neurons were observed in dorsal prosubiculum (ProS), a region between hippocampal dorsal CA1 (CA1d) and dorsal subiculum (SUBd) [11,12] (Fig. 1a). The distal part of CA1d (closest to ProS) and SUBd contained very few pTau+ pyramidal neurons at this age. The intensity of pTau in ProS peaked after 8 mo, with large numbers of pTau+ somata and processes (Fig. 1a,b), corresponding to the time when hippocampal-dependent memory deficits have first been observed.[9,13] Accordingly, a greater number of pTau+ neurons in CA1d were observed (Fig. 2), spreading towards CA2 and a corresponding increase in SUBd. Intensity of pTau decreased in aged mice (>16mo), likely due to cell loss [9] and a lack of pTau+ somata in ProS and SUBd of mice >21 mo (Fig. 1a,b). Based on the combination of changes in ProS and CA1, we define young mice as <8 mo, ageing mice as 8-16 mo, and aged mice as >16 mo.

In young mice, pTau+ dentate granule cells were rare at the septal pole (sparse pTau: n=4/5 mice; moderate pTau: n=1/5 mice) but common at the temporal pole (moderate or extensive: n=3/6 mice; absent or sparse: n=3/6 mice; Figs. 1a, S1a-c). Mossy fibers showed variable levels of pTau, likely originating from granule cells of the temporal pole (Fig. S1a,c). In ageing mice, the septal pole contained mostly moderate pTau (n=2/3 mice; sparse: n=1/3 mice) and the temporal pole more extensive pTau (n=2/3 mice; moderate: n=1/3 mice). In aged mice, the

85 septal pole was variable (moderate or extensive: n=5/10 mice; sparse: n=5/10 mice) whereas
86 the temporal pole showed extensive pTau (n=6/7 mice; sparse: n=1/6 mice; Figs. 1a, S1a-c).
87 Temporal (ventral) CA1 and CA3 also showed gradual increases in pTau levels during ageing
88 (Fig. S1c).

89 The most prominent and earliest site outside the hippocampal formation was the basolateral
90 amygdala, exhibiting moderate pTau at 2.5 mo and extensive pTau in all animals >4.5 mo
91 (n=14 mice; Figs. S1a, S2a-c). The medial prefrontal cortex showed modest pTau (Fig. S2a).
92 The entorhinal cortex had similar modest levels of pTau at all ages (Fig. S1d). In isocortical
93 areas, pTau was distributed primarily around layer 5, remaining sparse until much later in
94 life (sparse in n=10/10 young and ageing mice; moderate or extensive in n=7/9 aged mice;
95 Figs. 1c, S1a-c, S2b). In ntg littermates, pTau was not observed (n=16/16 mice, 2-24 mo).
96 Lipofuscin fluorescence was detected in all aged mice. In summary, the distribution in the
97 hippocampal formation, isocortex and amygdala largely confirmed previous reports.[9,13,14]

98 In contrast to the neuronal pTau distribution described above, key subcortical areas linked to
99 the generation of theta frequency rhythmic activity were unaffected, including anterior and
100 midline thalamus, medial septum (Fig. 1d, S2b,c), mammillary bodies, and supramammillary
101 nucleus. Other areas of the hypothalamus, and basal ganglia, were also largely unaffected
102 (Fig. S1a). In the midbrain, neuronal pTau was found in the red nucleus, deep layers of the
103 superior colliculus, periaqueductal gray, and pontine nuclei, but not in the raphe nuclei,
104 ventral tegmental area, substantia nigra, or interpeduncular nucleus (from n=4/4 aged mice).
105 Midbrain dopaminergic (tyrosine hydroxylase immunoreactive) neurons lacked pTau.
106 Furthermore, pTau+ axons were prominent in fimbria, fornix, lateral septum and thalamic
107 reticular nucleus, most likely originating from affected hippocampal/cortical neurons (Figs.
108 1d, S1a, S2b,c, 3a,b).

109 **Deep-layer CA1 pyramidal neurons preferentially accumulate pTau**
110 Hippocampal CA1 is critical for spatial/episodic memory and contains place cells. Neurons
111 containing pTau were immunoreactive for CTIP2, SATB2, and Wfs1, which are markers of
112 CA1 pyramidal cells [15,16] (n=50/51 pTau+ SATB2+ CA1d cells, n=3 mice; Fig. 2a-c).
113 Immunoreactivity for Wolframin (Wfs1) was extremely low compared to nearby unaffected
114 neurons and was localized to the plasma membrane (n=11/23 CA1d cells weakly
115 immunopositive, n=12/23 undetectable; Fig. 2c, S3a), suggesting that pTau affects Wfs1
116 levels.[17,18]

117 The upper, compact sublayer of stratum pyramidale (SP) primarily consists of calbindin
118 immunopositive (CB+) neurons, and the lower sublayer neurons are mostly CB
119 immunonegative (CB−, lacking detectable levels of CB).[16,19] Interestingly, the majority of
120 pTau+ CA1 SP neurons were found in the deep sublayer and were CB− (95 ± 6 % for n=3
121 young mice < 8 mo, n=3/52 CB+ pTau+ cells; 85 ± 5 % for n=3 ageing mice 8-14 mo, n=9/60
122 CB+ pTau+ cells; 79 ± 11 % for n=5 aged mice 16-23 mo, n=11/59 CB+ pTau+ cells; Fig. 2d).
123 Cells that were pTau+ lacked parvalbumin (PV) and calretinin (CR) immunoreactivity
124 (n=0/36 PV+ or CR+ cells from 2 mice), which mark subpopulations of GABAergic neurons.
125 In the ProS, most pTau+ cells lacked CB (n=0/30 CB+ in n=3 young mice, n=1/30 CB+ in n=3
126 ageing mice, n=3/47 CB+ in n=5 aged mice). We confirmed pTau in pyramidal neurons by
127 electron microscopy and also localized pTau to axon terminals (Fig. 2e). Thus, pTau
128 preferentially accumulated in CB− pyramidal neurons.

129 There is previous evidence of a general loss of CA1 cells in tg mice over 12 mo.[9] To determine
130 whether this was due to a loss of pyramidal neurons, we counted SATB2+ nuclei along CA1d
131 SP; SATB2 was not detectable in CA2 or ProS/SUBd pyramidal neurons. In aged mice, CA1
132 SP was markedly thinner, particularly towards ProS, where the most abundant pTau
133 inclusions were observed (Figs. 2f-h, 1a,b). There were fewer pyramidal cells in aged tg mice
134 compared to aged-matched ntg mice (34% reduction; mean ± s.d. 886 ± 9 nuclei for n=3 ntg
135 mice versus 585 ± 24 nuclei for n=3 tg mice; $t_{(4)}$=20.6, P< 0.0001; 22-23 mo; Fig. 2h). In contrast,
136 there was no difference in CA1 SATB2+ nuclei counts in young mice (426 ± 13 nuclei for n=2
137 ntg mice versus 483 ± 51 nuclei for n=2 tg mice; $t_{(2)}$=1.5, P=0.2643; 4-6 mo). Interestingly, we
138 did not find a difference in CA1 DAPI+ nuclei counts in ageing mice (659 ± 72 nuclei for n=2
139 ntg mice versus 555 ± 31 nuclei for n=2 tg mice; $t_{(2)}$=1.9, P=0.2020; 15-16 mo). Thus, we suggest
140 the accumulation of pTau in pyramidal neurons eventually leads to their degeneration in aged
141 mice.

142 **Spread of pTau from pyramidal neurons to oligodendrocytes**

143 In aged (n=11/11, 18-27 mo) and ageing (n=5/6, 8-16 mo) tg mice but not in young tg mice
144 (n=7/7, 2-6 mo), we observed coiled bodies – intensely AT8 immunoreactive 'flame-like' rings
145 of pTau – in many brain regions, especially in white matter tracts containing pTau+ axons
146 (Figs. 3, S4), such as the fimbria, fornix, alveus, dorsal hippocampal commissure, corpus
147 callosum, and stria terminalis. Coiled bodies were also in hippocampal stratum oriens,
148 subicular complex, granular retrosplenial cortex (Fig. S4), isocortex, dorsal striatum, lateral
149 septum, and were similar in appearance to those found in Alzheimer's disease.[20] The anterior
150 thalamus and mammillary bodies had scattered coiled bodies. In the brainstem, the substantia
151 nigra pars reticulata, ventral tegmental area, pontine nuclei and the interpeduncular nucleus
152 contained coiled bodies, a pathology found in 4R tauopathies such as CBD and PSP.[21,22]

153 Coiled bodies colocalized with Olig2, an oligodendrocyte transcription factor (Figs. 3, S4e,f).
154 Smaller coils (< 2 μm diameter) associated with Olig2-immunoreactive nuclei (Fig. 3c) may
155 represent densely packed pTau. Olig2 was not observed in pTau+ neurons (Fig. S4e). We
156 confirmed the presence of pTau+ filament bundles in oligodendrocytes using electron
157 microscopy (Fig. 3e).[23,24] To our knowledge, the Thy1 promoter is not active in
158 oligodendrocytes.[25] As coiled bodies were not observed in younger mice, despite
159 accumulation of pTau in neurons at all ages investigated (Fig. 1), we suggest pTau spreads
160 from neurons to oligodendrocytes via pTau-containing axons (Fig. 3).

161 **Reduced short-term familiarity but unimpaired spatial reference and working memory**

162 To test behavioral effects of pTau accumulation and neurodegeneration, we assessed short-
163 term hippocampal-dependent spatial memory (age range, 13-24 mo; median [interquartile
164 range] 15 [4] mo ntg, and 14 [5] mo tg mice) using a spontaneous spatial novelty preference
165 Y-maze task (Fig. 4a, STAR Methods). The total distance mice covered in the exposure phase
166 was similar for both genotypes (mean 1.78 ± s.d. 0.61 m for n=18 ntg mice versus 1.75 ± 0.45
167 m for n=15 tg mice; $t_{(31)}$=0.1635, P=0.8712; Fig. 4a), indicating tg mice were not hyper- or
168 hypoactive. Discrimination ratios (time in novel over total time in novel and other arms) were
169 significantly different (0.64 ± 0.10 for n=22 ntg mice versus 0.52 ± 0.16 for n=20 tg mice;
170 $t_{(40)}$=2.9637, P=0.0058; Fig. 4a). This was explained by ntg mice spending more time in the
171 novel arm compared to chance ($t_{(21)}$=6.6435, P< 0.0001; 110 ± 27 s novel arm, 61 ± 22 s other
172 arm), as expected for wild type animals.[26] Tg mice failed to discriminate ($t_{(19)}$=0.4840, P=0.6339;

84 ± 25 s novel arm, 85 ± 45 s other arm), consistent with previous studies reporting spatial novelty preference impairment in younger tg mice.[27,28]

To evaluate spatial reference memory, we tested 14 mo mice in a hippocampal-dependent water escape Y-maze task (Fig. 4b, STAR Methods).[29-31] Mice of both genotypes learned the location of the hidden platform. Tg mice performed similarly to ntg littermates during acquisition training (choice accuracy, repeated-measures two-way ANOVA: genotype $F_{(1,9)}$=0.1123, P=0.7452; training block $F_{(9,81)}$=6.809, P=0.0026; genotype x training block, $F_{(9,81)}$=0.9458, P=0.4908; Fig. 4b; one ntg mouse was excluded as it failed to make choices after day 3). On day 11, we removed the hidden platform and let mice swim freely for 60 s. We found no difference (58.6 ± 9.68% of time in the goal arm for n=4 ntg mice vs 64.56 ± 15.96%, n=7 tg mice; $t_{(9)}$=0.6660, P=0.5221; chance is 33.3% in the goal arm; Fig. 4b). In summary, based on this task we could not detect deficits in spatial reference memory.

We tested spatial working memory in a non-matching to place T-maze task (Fig. 4c, STAR Methods).[32] We tested mice at 4, 7 and 12 mo (n=11 ntg and n=16 tg mice; within-subject, longitudinal design) under mild food restriction to 90.7 ± 2.7% of their free-feeding weight. Behavioral performance improved with training (alternation score, repeated-measures ANOVA: training block $F_{(9,225)}$=8.497, P<0.001; Fig. 4c), independent of age and genotype (age $F_{(2,50)}$=0.534, P=0.590; genotype $F_{(1,25)}$=0.295, P=0.592; age x genotype $F_{(2,50)}$=0.024, P=0.976), with an overall similar performance across blocks (age x block x genotype $F_{(18,450)}$=0.522, P=0.948; Fig. 4c). Improvements in correctly alternating on the choice run occurred at all ages (Fig. 4c). All training was carried out within the same context; a new context would require mice to form new spatial maps, which might reveal differences in genotypes. One cohort (n=6 ntg and n=9 tg mice) was re-tested at 13 mo in a different context (STAR Methods). Mice approached a high alternation score by the 5th block for both genotypes (Fig. S5a).

During T-maze training we noticed that many mice would wait at the end of the start arm before voluntarily initiating a run. Strikingly, tg mice waited significantly longer than ntg mice before initiating their choice run (4 mo: 4.6 [3.9] s for ntg mice, 10.2 [11.1] s for tg mice, U=41, P=0.0218; 7 mo, 1.0 (4.1) ntg, 9.3 (12.3) s tg, U=23.5, P=0.0016; 12 mo, 5.1 (7.9) s ntg, 13.5 (14.0) tg, U=38, P=0.0145; Fig. 4d). However, this was also the case for the forced run (4 mo, 1.8 [1.4] s ntg, 3.8 [3.5] s tg, U=40, P=0.0191; 7 mo, 0.5 [1.3] s ntg, 3.2 [5.3] s tg, U=29.5, P=0.0042; 12 mo, 1.5 [3.1] s ntg, 6.9 [12.0] s tg, U=34.5, P=0.0089; Fig. S5b), suggesting the delay in choosing is not directly related to making decisions. Although ntg and tg mice had similar delay times in the first session (block 1), they rapidly diverged over subsequent days (Figs. 4d, S5b). Once mice left the end of the start arm, actual run times were similar, suggesting unimpaired ambulation (Fig. S5c). In summary, although we did not detect a spatial working memory impairment in this task, tg mice took longer to initiate both forced and choice runs.

Mice were also placed in an elevated plus maze, an ethological test of unconditioned anxiety. Wild type rodents tend to spend more time in closed than open arms, and time in open arms is increased in rats with ventral hippocampal lesions;[33,34] this region was also enriched with pTau (Fig. S1c). In young (3 mo) mice, tg mice spent a significantly greater proportion of time in open arms than ntg mice (17.1 [13.7] % of time in open arms for n=9 ntg mice versus 58.3 [29.9] % for n=5 tg mice; U=45, P=0.0022), consistent with previous reports at 6 mo.[9] There was also a slight difference in arm entries (12 [4.25] entries for 9 ntg mice versus 19 [7] for 5 tg mice; U=8, P=0.0448; Fig. 4e). In a separate cohort of 12 mo mice that had been extensively handled and tested in other behavioral tasks but were naïve to the plus maze, ntg mice (n=11)

spent 46.9 [16.4] % of time in open arms compared to 75.2 [34.0] % for tg mice (n=16) (U=142, P=0.0083; Fig. 4e). Taken together, we conclude that pTau aggregation affects short-term familiarity and anxiety-related activity but leaves spatial reference and working memory unimpaired.

Network oscillations are preserved in the presence of hippocampal pTau

To determine whether intracellular pTau affects neuronal and network activity, we used glass electrodes to record network oscillations and single neurons in the hippocampal formation of both awake head-fixed and freely moving mice. We first focused on 5-12 Hz theta oscillations, which reflect coordination of neuronal activity [35-38] required for spatial memory. Prominent theta oscillations were observed in aged (17-24 mo) head-fixed mice while they ran on a running disc (Fig. 5a), with similar peak theta frequency values across genotype for slow speeds (4-6 cm/s; 6.35 ± 0.59 Hz for n=3 ntg mice; 6.70 ± 0.45 Hz for n=3 tg mice; $t_{(4)}$ =0.947, P=0.3975) and faster speeds (6-10 cm/s; 6.70 ± 0.45 Hz ntg; 7.76 ± 0.60 Hz tg; $t_{(4)}$=2.454, P=0.0701). In a different context involving trained water-restricted aged mice (22-24 mo) running on an air-suspended jet ball along a virtual linear track, the theta peak was also similar for both genotypes (6.80 ± 0.16 Hz for n=3 ntg mice; 6.38 ± 0.27 Hz for n=3 tg mice; $t_{(4)}$=2.324, P=0.0808; Fig. 5a). These data suggest that the sampled theta frequency oscillations are unaffected by pTau.

In order to investigate potential network changes more closely, we compared the spectral content of local field potentials (LFPs) using empirical mode decomposition (EMD), which is more appropriate for non-linear non-stationary signals.[39,40] In aged mice (18-24 mo), we sampled LFPs recorded with glass electrodes and silicon probes for movement periods as above and used masked EMD to obtain intrinsic mode functions (IMFs; STAR Methods). Theta corresponded to IMF6 (Fig. 5c) with a mean instantaneous frequency of 7.3 ± 0.4 Hz in ntg mice (n=6) and 6.9 ± 0.2 Hz in tg mice (n=5). We detected slow-gamma (IMF4), mid-gamma (IMF3) and fast-gamma (IMF2) oscillations (Fig. 5c,d), with similar distributions for both genotypes (IMF4, 28.7 ± 0.7 Hz for n=6 ntg mice, 29.3 ± 1.2 Hz for n=5 tg mice; IMF3, 56.8 ± 0.8 Hz for n=5 ntg mice, 59.3 ± 4.1 Hz for n=4 tg mice; IMF2, 140.1 ± 6.3 Hz for n=6 ntg mice, 146.4 ± 4.3 Hz for n=5 tg mice; Figs. 5d, S6a).

Higher frequency oscillations are typically coupled to phases of slower oscillations in rodents and humans.[39,41] Impaired phase-amplitude coupling (PAC) has previously been attributed to pTau in mouse models,[35] and is altered in mild cognitive impairment and Alzheimer's disease.[42] Mid-gamma is associated with entorhinal inputs to CA1 superficial apical dendrites, detectable in CA1d SP at the peak of theta cycles in rodents.[43] Despite neurodegeneration and pTau (Fig. 2f-h), higher amplitude mid-gamma oscillations were detected close to the theta peak (n=4/4 aged tg mice, 18-23 mo; Figs. 5e, S6b,c). Similar results were observed in aged ntg mice (n=3/3, 20-24 mo) and ageing tg mice (mean IMF frequency distributions and PAC; n=2, 13-14 mo). Theta frequency was typically lower during the peak-to-descending phase of theta oscillations (Figs. 5e, S6b,c).

Memory consolidation is associated with another form of cross frequency coupling: the sharp wave ripple (SWR) complex, consisting of 130-230 Hz ripple oscillations occurring during ~30-120 ms sharp waves.[44] We detected ripples from CA1d SP in aged ntg and tg mice (18-24 mo) while they rested on the running disc (head-fixed) or in an open field. We found no difference between ntg (n=3) and tg (n=2) mice in terms of ripple frequency (124.7 ± 4.9 Hz ntg, 123.4 ± 4.6 Hz tg), ripple duration (53.1 ± 4.6 ms ntg, 51.7 ± 4.6 ms tg), or ripple cycle counts (6.6 ± 0.7

ntg, 6.3 ± 0.4 tg). Similar results were found for ageing tg mice (n=2, 13-14 mo). This suggests that the sampled CA1d SWRs are unaffected by pTau. In summary, our analysis of network oscillations suggests unimpaired neuronal coordination in the hippocampus, consistent with good performance in hippocampal-dependent spatial working and reference memory tasks.

Identification of single hippocampal neurons recorded in awake tg mice

After determining that local pTau did not affect network activity, we next investigated whether pTau disrupted the activity of individual neurons. To directly compare pTau+ and pTau− neurons, we performed extracellular recordings with glass electrodes in the hippocampal formation of head-restrained and freely-moving mice, followed by juxtacellular labeling (Fig. 6). We targeted the ProS, which contained high levels of pTau+ from an early age (Fig. 1). From a total of 47 recorded neurons (from n=8 aged tg mice, n=3 ageing tg mice and n=1 young tg mouse; 6-28 mo), we recovered 9 neurons (n=6 pyramidal neurons and n=3 interneurons). We tested 8 for AT8 (pTau) and all were immunonegative (Fig. 6d,e). We also recorded 20 single neurons in ntg littermates and wild type mice (from n=5 young mice, n=1 ageing mouse and n=1 aged mouse; 6-18 mo) and recovered 2 pyramidal neurons and 1 interneuron (Fig. 6a,b). Identified pyramidal cells in both tg and ntg mice were immunopositive for CTIP2 (Fig. 6b,e), matching the profile of pTau+ cells (Fig. 2a).

Under both freely-moving and head-fixed conditions, pyramidal neurons from both genotypes of all ages were recognized by relatively wide isolated spikes and complex spike (CS) bursts (Fig. 6a,c). Based on the locations, shapes and neurochemical profiles of the subset of recorded and labeled neurons (Fig. 6a-e) we could confidently classify unlabeled neurons with CS bursts as putative pyramidal cells, matching published data.[15,16] Our sample of glass electrode-recorded pyramidal neurons had a typical mean firing rate distribution, consisting of a majority of low firing cells and few high firing cells,[45] which broadly overlapped for the different age groups (Fig. 6f). Both genotypes had similar low firing rates (ntg rest, 0.92 [0.74] Hz, n=14 cells; tg rest, 0.69 [2.40] Hz, n=27 cells; U=191, P=0.9452; ntg movement, 0.17 [2.46] Hz, n=6 cells; tg movement 1.30 [3.45] Hz, n=22 cells; U=51, P=0.4132; Fig. 6f). Running speeds were also similar across genotype (medians of 6.14 versus 5.11 cm/s for ntg and tg mice, respectively; U=165, P=0.229).

Firing rates of labeled (identified) and unlabeled (putative) interneurons were typically higher than those of principal cells, lacked CS bursts, and showed a range of regular bursting activity and rhythmic firing patterns. Firing rates were also similar across genotypes (ntg rest, 11.53 [23.82] Hz, n=6 cells; tg rest, 13.17 [11.01] Hz, n=20 cells; U =58, P=0.9273; ntg movement, 18.95 [34.77] Hz, n=4 cells; tg movement 18.6 [12.05] Hz, n=19 cells; U =41, P=0.7765). Overall, the sampled range of firing rates of the recorded principal cells and interneurons in tg mice were similar to ntg littermates and other wild type (wt) mice (Fig. 6g).

Fewer high-firing pyramidal neurons in aged transgenic mice during goal-directed navigation

Next, we investigated whether pTau affected neuronal activity when mice were engaged in a goal-directed navigation task. We trained water-restricted aged head-fixed mice to run on an air-suspended jet ball along a virtual linear track to reach a water reward. From 16 aged mice, of which 9 had previously been used in spatial memory tests, 11 could be successfully trained to run with a stable gait to the end of the corridor and initiate licking (n=6/9 tg and n=5/7 ntg mice; Table S1). Mice ran 45 ± 34 trials per session (1-4 sessions per mouse, with a maximum of 136 trials over 1 session for a tg mouse). For sessions with good coverage (>12 trials, 92% of

all sessions), mice had similar trial durations (47 [64] s per trial across n=9 sessions for ntg mice versus 34 [30] s per trial across n=15 sessions for tg mice; U=41, P=0.1074). During this task we recorded multiple unit activity with acute silicon probes, unilaterally targeting ProS. We isolated 308 units (n=119 from 5 ntg mice, 16-24 mo; n=189 from 5 tg mice, 18-23 mo), localizing 147 units to ProS/SUB and 161 to adjacent CA1d (Table S1).

First we compared firing rates of all units that had complex spikes (CS) – putative pyramidal cells – matching the patterns of the recorded and labeled pyramidal neurons (Fig 6). There were no differences in mean firing rates between genotype (mean ± standard error 4.7±1.2 Hz for n=85 units from 5 ntg mice; 2.7±1.1 Hz for n=132 units from 5 tg mice; linear mixed model, mouse as a random factor, genotype fixed effect: $F_{(1,3.1)}$=1.492, P=0.3072; Fig. 7a) or recording region (3.4±0.9 Hz for n=97 units from ProS/SUB; 4.0±1.0 Hz for n=120 units from CA1; region fixed effect: $F_{(1,13.6)}$=0.378, P=0.5490). However, we found a significant difference for the interaction between genotype and region (5.5±1.3 Hz in ProS/SUB, n=39 units from 3 ntg mice; 1.3±4.0 Hz in ProS/SUB, n=58 units from 3 tg mice; 3.9±1.2 Hz in CA1, n=46 units from 4 ntg mice; 4.2±1.5 Hz in CA1, n=74 units from 3 tg mice; genotype-region fixed effect: $F_{(1,13.6)}$=4.990, P=0.0428; Fig. 7b, Table S1). The distributions were also significantly different for ProS/SUB but not CA1 (pooled data per region, ProS/SUB ntg versus tg: D=0.3563, P=0.0037; CA1 ntg versus tg: D=0.1645, P=0.3751; Fig. 7b). These results suggest that there are fewer high-firing cells in ProS/SUB in aged tg mice.

Previous studies have set firing rate thresholds to help separate putative pyramidal cells (assumed to be low-firing) from high-firing interneurons.[46] When we compared low-firing ntg and tg CA1 CS units (mean firing rates < 3 Hz) to a separate dataset obtained from younger wt mice performing a similar task on the same jet ball,[43] we found no difference in firing rates (mean ± standard error 0.9±0.2 Hz, n=29 ntg units; 1.1±0.2 Hz, n=55 tg units; 1.1±0.1 Hz, n=159 wt units; linear mixed model, mouse as a random factor, genotype fixed effect: $F_{(2,9.6)}$=0.6835, P=0.5278; Table S1, Figs. 7c,d, S6d). This suggests that for the subpopulation of low-firing pyramidal cells, aged mice have similar firing rate distributions to younger mice. Since we have identified high-firing (> 3 Hz) CS cells as pyramidal cells in ProS, SUB and CA1 (Fig. 6), we suggest higher firing ProS/SUBd pyramidal cells, which could have special roles distinct from other cells,[45] are preferentially lost in tg mice, leaving the lower firing CS cells.

We also compared firing rates of units that lacked CS – putative interneurons – matching the profiles of some of the recorded and labeled interneurons. In contrast to CS cells, there were no significant differences in firing rates across genotype, region or their interaction (mean ± standard error 16.1±4.3 Hz for n=29 units from 5 ntg mice; 9.1±3.8 Hz for n=62 units from 5 tg mice; linear mixed model, mouse as a random factor, genotype fixed effect: $F_{(1,7.5)}$=1.530, P=0.2532; 12.6±3.3 Hz for n=50 units from ProS/SUB; 12.6±3.4 Hz for n=41 units from CA1; region fixed effect: $F_{(1,42.8)}$=0.0003, P=0.9874; 14.0±4.9 Hz in ProS/SUB, n=12 units from 3 ntg mice; 11.2±4.4 Hz in ProS/SUB, n=38 units from 3 tg mice; 18.3±4.6 Hz in CA1, n=17 units from 4 ntg mice; 6.9±4.9 Hz in CA1, n=24 units from 3 tg mice; genotype-region fixed effect: $F_{(1,42.8)}$=1.534, P=0.2222; Fig. 7a, Table S1). The proportions of CS versus non-CS units were also similar across genotype (mean ± s.d. 76±17% CS units, n=5 sessions for ntg mice; 62±18% CS units, n=5 sessions for tg mice; excluding sessions with <14 units; U=18, P=0.2963; Fig. 7a, Table S1).

We also investigated whether reduction of high-firing ProS/SUB CS units in tg mice affected the relative proportion of place cells (Fig. 7c,d), which represent different locations of the

353 virtual linear track.[47] Ntg and tg mice had fairly similar proportions of place cells (17.5%
354 (20/114 units), n=5 ntg mice; 25.3% (49/194 units), n=5 tg mice). Place fields were observed at
355 different locations along the virtual corridor, with some associated with the reward (goal
356 location, Fig. 7c,d). Interestingly, some units showed synchronized firing following reward
357 periods (e.g. units u1586 and u3770, Fig. 7d). These data suggest that place cell mapping is
358 preserved in these aged tg mice.

359 **Preservation of theta rhythmicity in aged mice**

360 Given that we did not detect any major differences in theta oscillations or other associated
361 spectral components (Fig. 5), we hypothesized that the remaining neurons in aged tg mice
362 would retain their theta coupling, despite extensive pTau. Indeed, units from tg mice were
363 coupled to theta and could become synchronized on individual theta cycles within
364 overlapping place fields (Figs. 7d,e, S6d-f). For CS units, 95% from ntg mice (n=80/84 units)
365 and 86% from tg mice (n=107/125 units) were significantly theta coupled (Rayleigh tests,
366 $P<0.05$; Fig. 7c-f). There were no differences in theta coupling across genotype or region (mean
367 ± standard error vector length r=0.21±0.013 for n=80 units from 5 ntg mice; r=0.22±0.011 for
368 n=107 units from 4 tg mice; linear mixed model, mouse as a random factor, genotype fixed
369 effect: $F_{(1,1.1)}=0.580$, $P=0.580$; r=0.15±0.032 for n=59 units from ProS/SUB; r=0.24±0.024 for
370 n=128 units from CA1; region fixed effect: $F_{(1,1.4)}=0.239$, $P=0.690$; Fig. 7e). The most strongly
371 coupled CS units for ntg and tg mice were r=0.47 and r=0.64, respectively; both were found
372 within SUBd. We also found no difference in the distributions with respect to theta coupling
373 versus firing rate ($D=0.4458$, $P=0.0994$; Fig. 7f). The phase distribution (spread) was greater in
374 aged tg mice (circular standard deviation of angles, ProS/SUB: 40° for ntg mice (n=25 units)
375 versus 71° for tg mice (n=34 units); CA1: 61° for ntg mice (n=55 units) versus 100° for tg mice
376 (n=72 units); Fig. S6e). Furthermore, for the subsets of theta-coupled CS units with firing rates
377 <3 Hz and significant phase coupling, coupling strength was no different from data obtained
378 from younger wt mice [43] (mean ± standard error vector length r=0.21±0.015 for n=32 units
379 from 4 ntg mice; r=0.23±0.011 for n=57 units from 3 tg mice; r=0.20±0.010 for n=152 units from
380 6 wt mice; linear mixed model, mouse as a random factor, genotype fixed effect: $F_{(2,7.7)}=0.988$,
381 $P=0.415$).

382 For non-CS cells, 94% from ntg mice (32/34 units) and 85% from tg mice (50/59 units) were
383 significantly coupled to theta oscillations (Rayleigh tests, $P<0.05$). As with CS units, there were
384 no differences in coupling strength of non-CS units across genotype (mean ± standard error
385 vector length r=0.19±0.034 for n=32 units from 5 ntg mice; r=0.19±0.027 for n=50 units from 5
386 tg mice; linear mixed model, mouse as a random factor, genotype fixed effect: $F_{(1,6.2)}<0.001$,
387 $P=0.987$; Fig. 7e) or in the distributions of coupling versus firing rate ($D=1.1272$, $P=0.6191$; Fig.
388 7f). However, we detected significantly different coupling in ProS/SUB versus CA1
389 (r=0.15±0.032 for n=29 units from ProS/SUB; r=0.24±0.024 for n=53 units from CA1; region
390 fixed effect: $F_{(1,13.0)}=5.524$, $P=0.035$), suggesting that interneurons in CA1 are more strongly
391 coupled overall. As for CS units, the phase distribution of non-CS units was also greater in
392 aged tg mice (ProS/SUB: 49° for ntg mice (n=9 units) versus 82° for tg mice (n=20 units); CA1:
393 44° for ntg mice (n=23 units) versus 71° for tg mice (n=30 units); Fig. S6f). In summary, we
394 could detect no differences in theta phase coupling in aged ntg and tg mice.

395 Discussion

396 We found an age-related progression of pTau, consistent with previous reports,[9,13,14,48] and
397 other Thy1 promoter-driven 4R Tau lines.[49-51] We further mapped pTau up to 28 mo, finding

398 that deep-layer Wfs1+/CB– hippocampal pyramidal neurons preferentially accumulated
399 pTau, followed by neurodegeneration. The apparent downregulation of the transmembrane
400 glycoprotein Wfs1 in pTau+ pyramidal cells could be related to its role in regulating
401 degradation of misfolded proteins in the endoplasmic reticulum, highlighting susceptibility
402 to neurodegeneration.[18] Oligodendrocytes also became pTau+ and were associated with
403 pTau+ white matter tracts. We suggest the extensive Tau pathology in the hippocampal
404 formation and loss of higher firing ProS cells contributed to specific deficits in short-term
405 familiarity. We did not detect impairments in network oscillations or theta coupling, and
406 spatial working and reference memory performance were similar for tg and ntg mice.

407 *Mechanisms and consequences of pTau spreading to oligodendrocytes.* The pTau+ coiled bodies we
408 found in oligodendrocytes resemble those in PSP, CBD and Alzheimer's disease,[20-22,52] and are
409 probably a feature specific to overproduction of 4R pTau.[53] Coiled bodies may facilitate pTau
410 propagation in humans, as mice inoculated with pTau from tauopathy model mice or patients
411 exhibit spreading via oligodendrocytes.[54-56] This makes THY-Tau22 mice a useful model for
412 aspects of PSP and CBD. As Thy1 is neuron-specific,[25] we suggest pTau within axons spreads
413 directly to oligodendrocytes. Alternatively, Thy1 in oligodendrocytes could be repressed in
414 younger animals; examining aged Thy-GFP mice for GFP+ oligodendrocytes may be
415 informative. Oligodendrocytes containing pTau along fiber tracts strongly suggests entry at
416 paranodal septate-like junctions between the axonal membrane and myelin adjacent to the
417 nodes of Ranvier,[57] which could then spread to the cell body.[58] In the *MAPT*^{P301S} tauopathy
418 model, new oligodendrocytes increase at 5-6 mo prior to onset of cognitive deficits, which has
419 been suggested to compensate for an early loss of myelin.[59] Disruption of oligodendrocyte
420 precursor cells causes memory impairments.[60] Conversely, promotion of oligodendrogenesis
421 in aged mice is associated with memory improvement.[61] In THY-Tau22 mice, it is possible that
422 disruption of myelin production affects action potential propagation. Myelinating satellite
423 oligodendrocytes [24] are tightly associated with neuronal somata, and are electrically coupled
424 to astrocytes and other oligodendrocytes.[62] As we have observed coiled bodies close to pTau+
425 pyramidal neurons, and fewer higher firing pyramidal cells in aged tg mice, disruption of
426 gray matter oligodendrocytes could also contribute to the reduction in higher firing activity
427 and affect spike initiation and/or propagation. Anterograde transneuronal pTau spread is
428 unlikely as we did not observe pTau in regions innervated by abundant pTau+
429 ProS/SUBd/CA1d pyramidal neurons such as lateral septum, anterior thalamus or
430 mammillary bodies. However, ProS projects to the amygdala,[11] and both regions were highly
431 enriched in pTau.

432 *Unimpaired cortical neuronal coordination and spatial memory.* Theta-coupled bursting
433 GABAergic neurons of the medial septum (MS) project to the temporal cortex,[63-65] and MS
434 inactivation reduces cortical theta power and impairs spatial memory.[36,66-69] Disruption of MS
435 cholinergic neurons by pTau can also cause memory deficits,[70] and a cholinergic deficit was
436 reported in THY-Tau22 mice.[27] Selective inactivation of rat anterior or ventral midline
437 thalamic nuclei also results in spatial memory impairments;[71,72] several of these nuclei also
438 contain theta-rhythmic neurons and project to temporal cortical areas. We did not detect
439 pTau+ neurons in the MS or thalamus, which could explain why theta coupled neurons, theta
440 peak frequencies, IMFs, and cross-frequency coupling in heavily pTau-dominated CA1-SUB
441 had broadly similar distributions for both genotypes under our conditions. We used
442 longitudinal behavioral testing at different ages. This may have acted as an enriched
443 environment, which is known to delay onset of memory deficits.[73] Also, spatial learning can

lead to neuroprotective oligodendrogliogenesis.[60] Many behaviorally-tested animals were used for the neurophysiological recordings. Previous studies reporting that 9-10 mo tg mice spend longer finding the hidden platform in a Morris water maze also found they had increased thigmotaxis,[13,28] with deficits emerging as early as 3 mo.[9] We minimized this potential confound by using a water escape Y-maze,[29] revealing tg mice are unimpaired for spatial reference memory. In summary, unimpaired hippocampal neuronal coordination may largely explain why we observed normal hippocampal-dependent spatial reference and working memory performance.

Reduction in short-term familiarity. We found that >13 mo tg mice failed to discriminate novel and other arms of the hippocampus-dependent [74] spontaneous spatial novelty preference Y-maze, as shown previously in younger mice.[27,28] This suggests impairment in recognizing familiarity of extra-maze spatial cues, which are required for spatial novelty preference.[75] Encoding and recall of spatial memories involves coordination of sequential neuronal activity within and between different brain regions. Compared to CA1, the SUBd contains a richer variety of spatially-modulated neurons including head direction cells, boundary vector cells, grid cells, as well as place cells,[72,76] and unlike CA1, receives direct glutamatergic input from the anterior thalamus. The loss of higher firing neurons in ProS/SUBd, due to high pTau levels, suggests sequences of neurons encoding different features of the environment may be disrupted. A reduction in short-term familiarity could also explain why tg mice spent significantly longer in the start arm of the T-maze before initiating runs: placement in the start arm retained some novelty for the mouse, possibly due to the reduction in ProS/SUBd activity. Lastly, we found that both young and ageing tg mice naïve to the elevated plus maze spent longer in the open arms. The ventral hippocampus and inter-connected amygdala also develop early Tau pathology,[14] which we observed throughout the lifetime of the tg mice. Furthermore, lesions of rat ventral hippocampus alters anxiety-related contextual behavior but not spatial learning.[77,78] Taken together, changes in spatial familiarity may be explained by potential deficits of different kinds of spatially-modulated cells within pTau-enriched ProS/SUBd.

Effects of pTau on identified neurons. Our single recorded and labeled neurons lacked pTau, hence we do not know how pTau affects *in vivo* firing, but in aged tg mice there were fewer higher firing ProS pyramidal cells during goal-directed navigation. In addition to neurodegeneration in aged mice and potential disruption of axon potential propagation by pTau+ oligodendrocytes, it is also possible that local pTau accumulation within pyramidal neurons causes a reduction in firing rate, contributing to the shift in the distribution to lower rates. To our knowledge, there are no reports on *in vivo* firing of single hippocampal neurons that specifically accumulated pTau. In the rTg4510 tauopathy model, mice have slower membrane potential oscillations and reduced firing rates, but only one labeled pTau+ neocortical neuron was reported.[37] *In vivo* calcium imaging in 6-12 mo rTg4510 mice show diminished activity under anesthesia.[79] These lower activity levels could be attributed to an actual loss of higher firing cells, shifting the populations towards lower firing cells. Matching pTau content to imaged/recorded neurons is needed to test the effects of pTau on neuronal activity. In 3 male 3xTg mice, hippocampal place cells had reduced firing rates, lower place field stability and less spatial information compared to wt mice, which was attributed to abnormal theta and gamma oscillations.[80] We did not record multiple place cells under freely moving conditions so do not know whether THY-Tau22 mice also exhibit similar deficits,

489 although mutant Tau in combination with induced amyloid-beta plaques and potential extra-
490 hippocampal transgene expression may have contributed to deficits in the 3xTg model.

491 Skewed firing rate distributions are a common feature of the brain, with the high-firing
492 minority having key roles, tending to be more highly connected, and able to generalize across
493 different contexts.[45,81] A loss of strongly-potentiated higher firing cells would presumably
494 result in an overall shift of the firing rate distributions towards a lower median. In acute slices,
495 long term potentiation in CA1 was similar in tg and ntg mice, despite lower synaptic
496 excitability in ageing tg mice.[9] Chronic high-density recordings in ageing mice would be
497 required to determine whether synaptic plasticity in lower firing cells largely compensates for
498 the loss of highly potentiated synapses. The effect on spatial navigation could be that mice
499 take longer to recognize contexts due to a loss of 'generalizer' high-firing neurons.
500 Nevertheless, spatial memory *per se* is retained due to unimpaired neuronal coordination
501 (such as spike timing during theta oscillations). Alzheimer's disease, FTDP, PSP and other
502 tauopathies show Tau pathology in several subcortical areas such as the thalamus and
503 brainstem, which could promote memory deficits. Overall, the results of our detailed
504 characterization of the THY-Tau22 mouse line demonstrate that in spite of widespread
505 hippocampal Tau pathology, uptake of pTau by oligodendrocytes, neurodegeneration, and
506 loss of high firing ProS/SUBd cells, many measured functional parameters and behaviors
507 remain remarkably similar to age-matched control animals, likely due to the operations of
508 unaffected neuronal systems.

509 *Limitations of the study.* Since we recorded mostly in CA1d and ProS/SUBd, we cannot rule
510 out changes in network oscillations and neuronal activity in other pTau-rich regions.[82] We
511 recorded place cells in head-fixed mice running along a virtual linear track. Establishing
512 whether other kinds of spatially modulated cells are affected by pTau requires high density
513 recordings in ProS/SUBd of freely moving aged tg mice. To directly compare pTau+ and
514 pTau– neurons, *in vivo* calcium imaging experiments could be performed followed by *post-hoc*
515 immunohistochemical tests for pTau matched to the imaged neurons, as we carried out for
516 single recorded and juxtacellularly labeled cells.

517 Acknowledgements

518 This study was supported by the Medical Research Council (MR/R011567/1), Alzheimer's
519 Society (522 AS-PhD-19a-010), Wellcome Trust (108726/Z/15/Z), Erasmus+, and the Nuffield
520 Benefaction for Medicine and the Wellcome Institutional Strategic Support Fund (0007268).
521 We thank Luc Buée and INSERM for kindly providing THY-Tau22 mice, Vitor Lopes dos
522 Santos for advice on EMD, Balint Lasztoczi for published recording data, Emily Hunter and
523 Verena Gautsch for assistance with histology, and Sawa Horie and Katalin Lengyel for
524 providing training to B.S. for electron microscopy. We thank Alex Jeans for commenting on
525 an earlier version of the manuscript.

526 Author contributions

527 Conceptualization: T.J.V., B.S., A.T.O., K.H., J.S., D.B., P.S.; Methodology: T.J.V., B.S., A.T.O.,
528 K.H., J.S., D.B., P.S.; Investigation: T.J.V., B.S., A.T.O., K.H., J.S., D.B., P.S.; Writing – Original
529 Draft: T.J.V.; Writing – Review & Editing: T.J.V., B.S., A.T.O., K.H., J.S., D.B., P.S.; Funding
530 Acquisition: T.J.V., P.S.; Supervision: T.J.V., A.T.O., P.S.

Declaration of interests

The authors declare no competing interests.

Figures

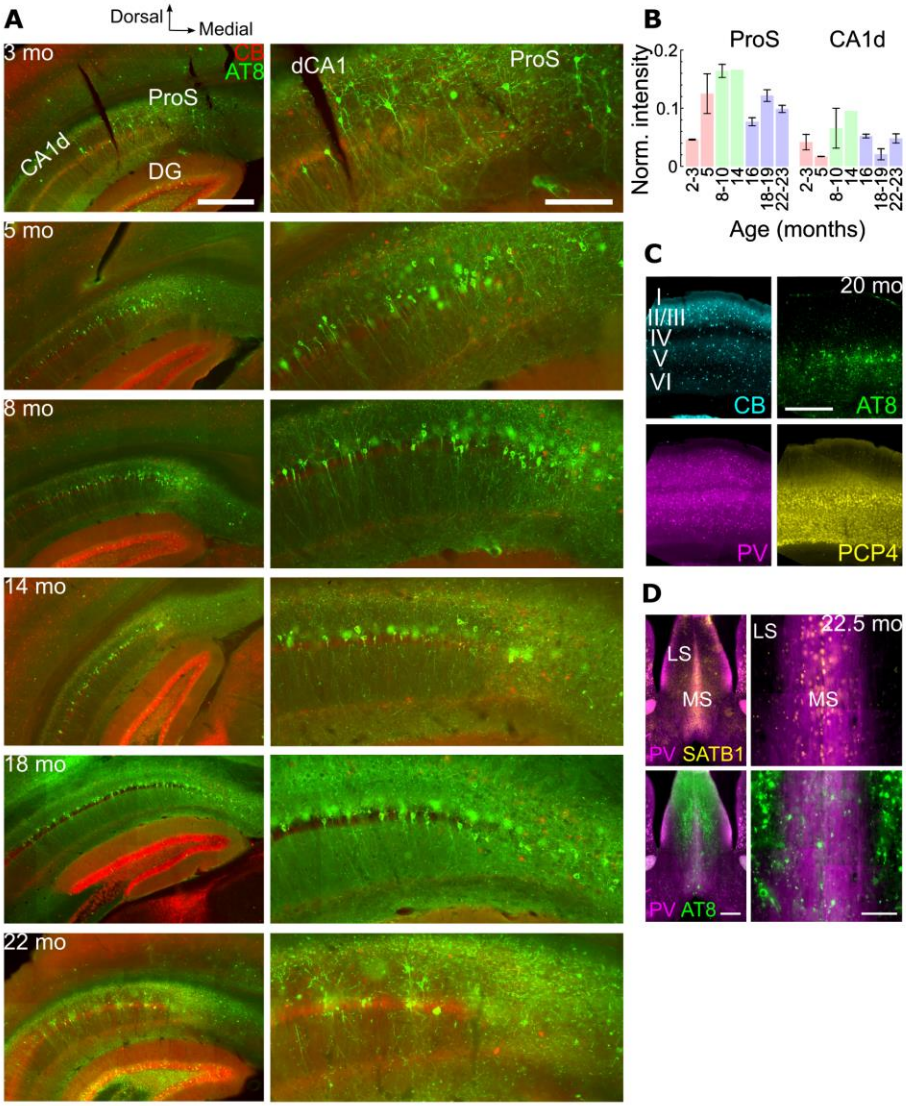

Figure 1. Age-related increase of pTau in THY-Tau22 mice.
(A) Immunoreactivity for AT8 (pTau+, green) in coronal sections containing the hippocampal formation at different ages (months old, mo). Calbindin (CB, red). Right, enlarged views of distal CA1 (dCA1) and dorsal prosubiculum (ProS). Widefield epifluorescence. **(B)** Normalized intensity measurements of AT8 immunoreactivity (mean, standard error) at 6 different age ranges in ProS and dorsal CA1 (CA1d). Age ranges (left to right): young (pink), 2-3 mo (n=2) and 5 mo (n=2); ageing (green), 8-10 mo (n=2) and 14 mo (n=1); aged (purple), 16 mo (n=2), 18-19 mo (n=2) and 22-23 mo (n=2). **(C)** Immunoreactivity for pTau (green) in deep cortical layers at 20 mo relative to CB (cyan), parvalbumin (PV, magenta) and Purkinje Cell Protein 4 (PCP4, yellow) immunopositive subpopulations. **(D)** Lack of pTau in the medial septum (MS) in a 23 mo tg mouse (case TT21D, female). Processes containing pTau found mostly within lateral septum (LS). Left, epifluorescence tile showing PV (magenta) and SATB1

547 (yellow) restricted to the MS. Right, enlarged view, note AT8 (green) mostly in LS. Scale bars
548 (µm): A (left), 500; A (right), 200; C, D (left), 500; D (right), 100. Cases in A, top to bottom
549 (mouse, sex): TT114A m; TV132 m; TV143 m; TV136 f; TV139 m; TT33G f.

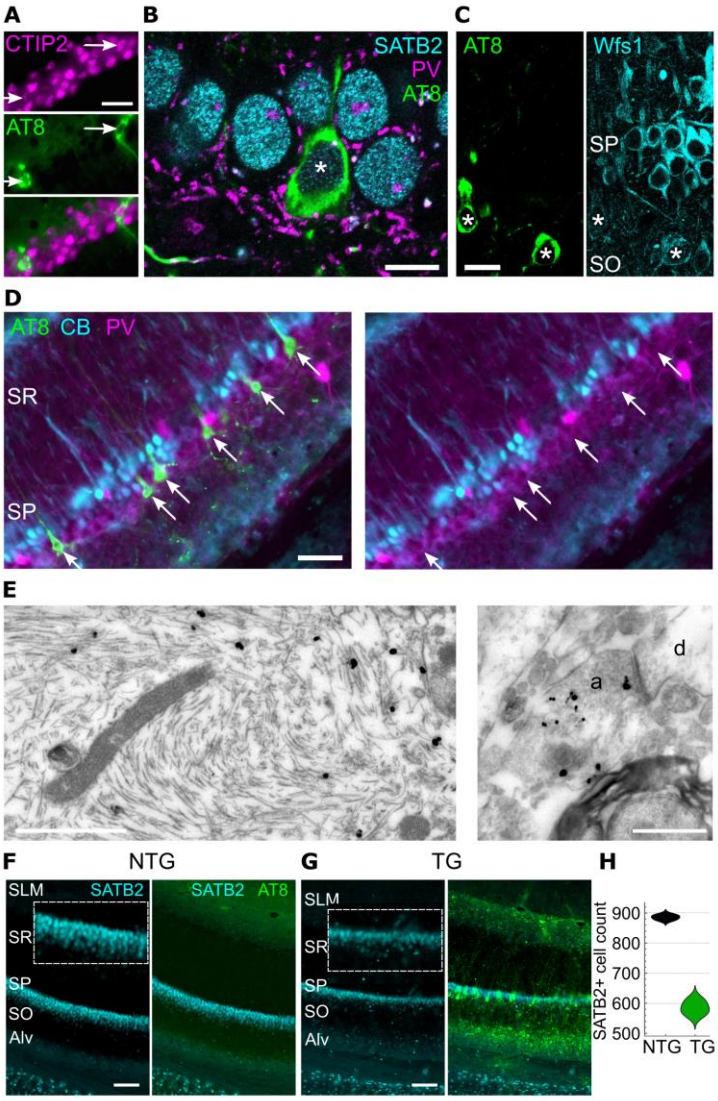

550

551 **Figure 2. Preferential accumulation of pTau in deep-layer CA1 pyramidal cells.**
552 **(A)** Neurons immunoreactive for pTau (AT8, green, arrows) in an ageing mouse show nuclear
553 immunoreactivity for CTIP2 (magenta) in CA1d SP. Widefield epifluorescence, case TV136
554 (14 mo). **(B)** A pTau+ neuron (asterisk) in distal CA1d SP immunopositive for SATB2 (cyan)
555 in an aged mouse. Note PV+ basket terminals around somata (magenta). Confocal single
556 optical section (0.43 µm thick), case TT21D (23 mo). **(C)** Weak Wfs1 immunoreactivity (cyan)
557 in pTau+ distal CA1d neurons (AT8, green, asterisks) in a young mouse. Confocal single
558 optical section (1 µm thick), case TV133 (6 mo). **(D)** Cells in CA1d SP immunopositive for pTau
559 (AT8, green). Lack of detectable CB (cyan) or PV (magenta) immunoreactivity in pTau+
560 neurons within deep SP (arrows). Widefield epifluorescence. **(E)** Electron micrographs of
561 AT8-positive filaments (gold-silver particles) within a cell body (left) and an axon terminal (a,
562 right). Dendrite, d. From an aged mouse (case TT33G, 21 mo female). **(F, G)** Immunoreactivity
563 of SATB2 (cyan) and AT8 (green) in CA1d of aged ntg and tg mice (22 mo). Insets, enlarged

views of SP. Widefield epifluorescence. **(H)** Distribution chart of SATB2+ nuclei counts in CA1d (n=3 mice/genotype). Alveus, Alv; stratum oriens, SO; stratum radiatum, SR; stratum lacunosum moleculare, SLM. Scale bars (µm): A, C, 20; B, 10; D, 50; E, 0.5; F, G, 100.

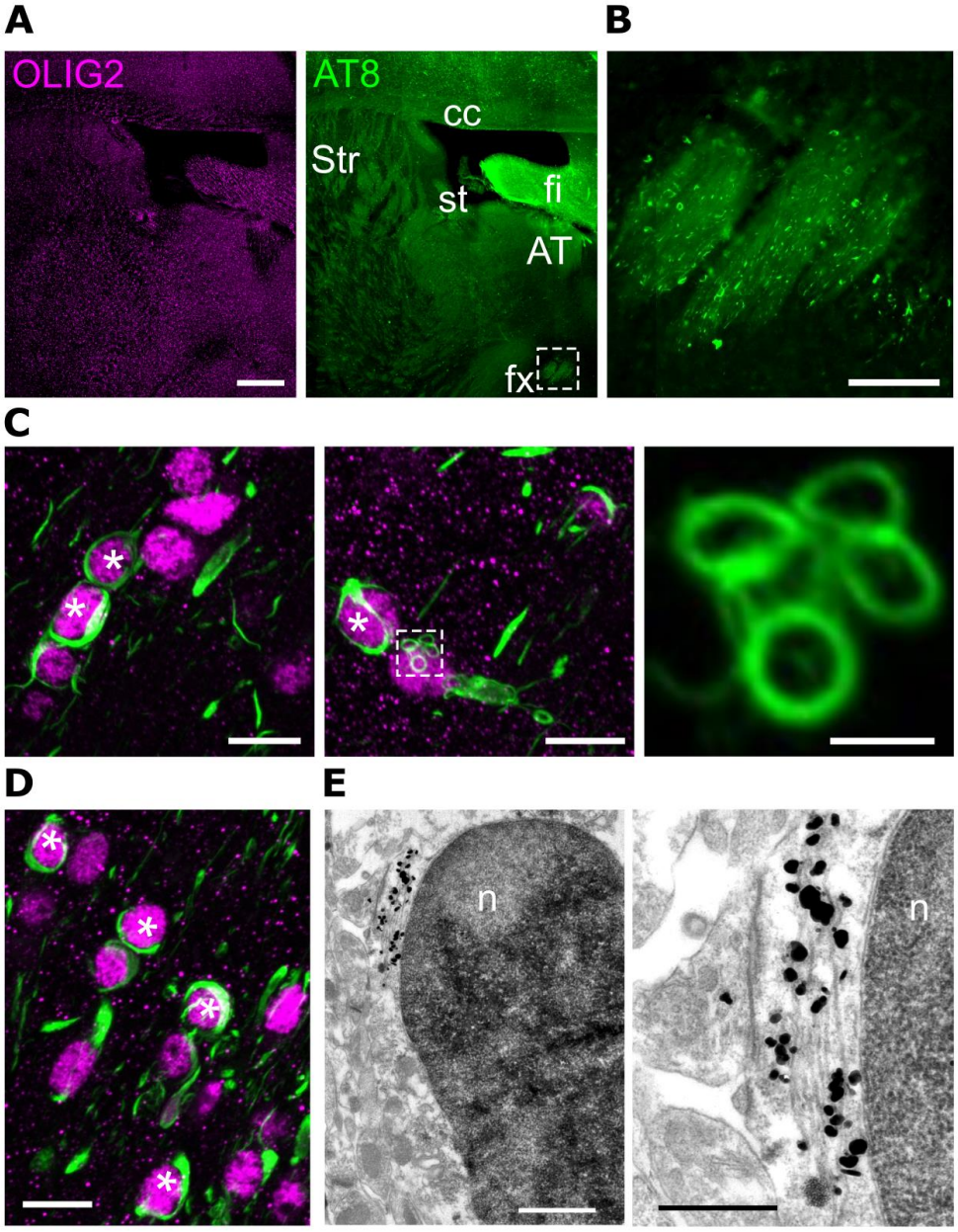

Figure 3. Accumulation of pTau in oligodendrocytes.
(A) Olig2 (magenta) and pTau (AT8, green) from an aged (20 mo) tg mouse (widefield epifluorescence). Note high density of pTau in fimbria (fi). **(B)** Enlarged view of boxed region from A of the fornix (fx), showing neuropil threads (axons) and coiled bodies. **(C)** Nuclear immunoreactivity for Olig2 (magenta, asterisks) surrounded by coiled bodies (green, AT8). Right, enlarged view of 'microcoils' near an Olig2+ nucleus (boxed region, middle panel). **(D)** Coiled bodies colocalizing with Olig2+ nuclei in the fimbria. **(E)** AT8-positive filaments (gold-silver particles) in the cytoplasm of an oligodendrocyte in the ProS next to an Olig2-immunolabeled nucleus (n) (peroxidase labeling) from an aged mouse (case TT21D, 23 mo). Right, higher magnification. Abbreviations: Str, dorsal striatum; cc, corpus callosum; st, stria

terminalis; AT, anterior thalamus. Scale bars (µm): A, 500; B, 100; C, 10, 10, 2; D, 10; E, 0.5. Confocal maximum intensity z-projection thickness (µm): C, 4, 9.6, 2.4; D, 4.

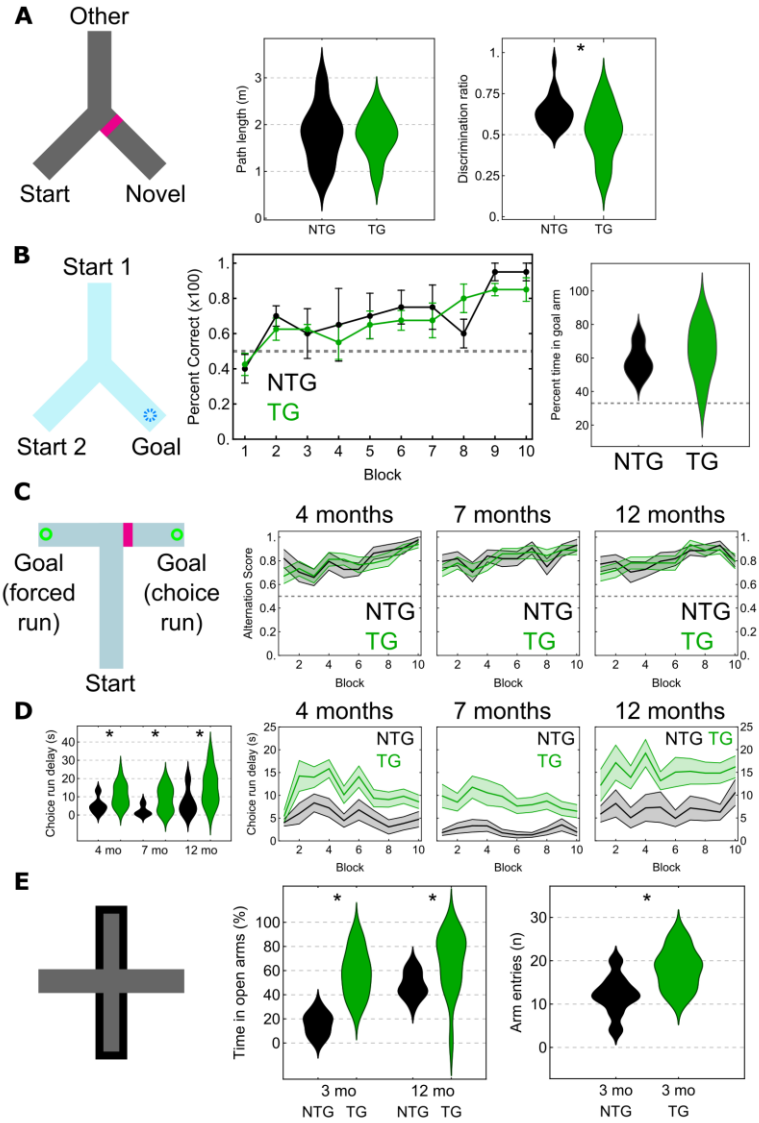

Figure 4. Selective impairments in spatial novelty preference.
(A) Short-term spatial novelty preference Y-maze test. Left, schematic (extra-maze cues not shown). Novel arm is blocked off for exposure phase and block removed for test phase (magenta bar). Middle, total distance traveled during test phase. Right, distribution chart for discrimination ratio; dashed line, no discrimination (0.5, chance). **(B)** Water escape Y-maze task. Left, schematic: two possible start arms and a goal arm containing a hidden platform submerged in opaque water. Middle, mean values for % correct over time (blocks). Error bars, standard error. Right, distribution chart for probe test. Dashed lines, chance. **(C)** Non-matching to place T-maze task. Left, schematic: start arm and rewarded goal arms. In choice run, block (magenta bar) is removed. Mean alteration scores over time (blocks) for each age. Error bands, standard error. Dashed line, chance. **(D)** Left, distribution chart of mean choice run delay times (ntg, black; tg, green) during training in T-maze at 4, 7, and 12 mo. Right, mean and standard error across blocks. See Fig. S5b for forced run delay times. **(E)** Elevated plus-maze with open and closed arms (left). Distribution charts for % time in open arms

(middle) and number of arm entries (right). Asterisks in A, D, E: significant differences. Abbreviations: mo, months old; NTG, non-transgenic; TG, transgenic mice.

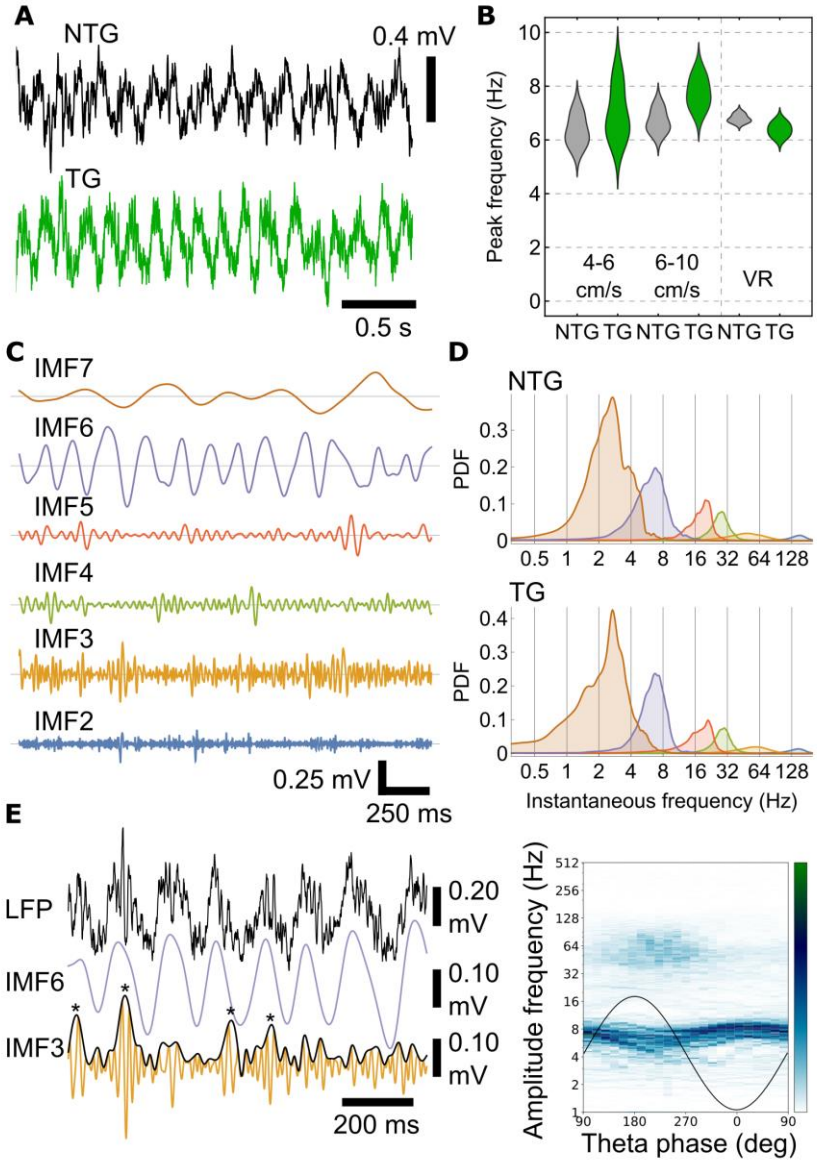

Figure 5. Similar hippocampal network oscillations in tg and ntg mice.
(A) LFP during movement for aged littermates (ntg mouse, black, case TV140; tg mouse, green, case TV139; 18 mo). **(B)** Distribution chart of peak theta frequencies for two speed bins during spontaneous movement on a running disc, and during navigation in virtual reality (VR), for aged mice. **(C)** Empirical mode decomposition of glass electrode LFP in CA1d SP during movement (aged ntg mouse, 23 mo, case TV147). Theta (IMF6), slow-gamma (IMF4), mid-gamma (IMF3) and fast-gamma (IMF2) oscillations; IMF7 likely corresponds to 'delta' and IMF5 to 'beta'. **(D)** Probability density functions (PDF) of instantaneous frequency for the 7 IMFs. Top, aged ntg mouse (23 mo, case TV147). Bottom, aged tg mouse (18 mo, case TV139). Note similar distributions and spectral peaks. **(E)** Left, unfiltered wideband LFP from an ageing tg mouse (13 mo, case TV136) with IMF6 (purple, theta) and IMF3 (orange, mid-gamma). Black curve, instantaneous amplitude for IMF3; note higher amplitude near peaks of some theta cycles (asterisks). Right, co-modulogram of a 30 s movement epoch binned for

IMF6 (theta) phase. Note phase amplitude coupling for mid-gamma (IMF3) around peak-to-descending theta phase. Theta frequency also modulated by phase. Black curve, sinusoidal schematic theta cycle. Color bar: green, maximum; white, minimum amplitude.

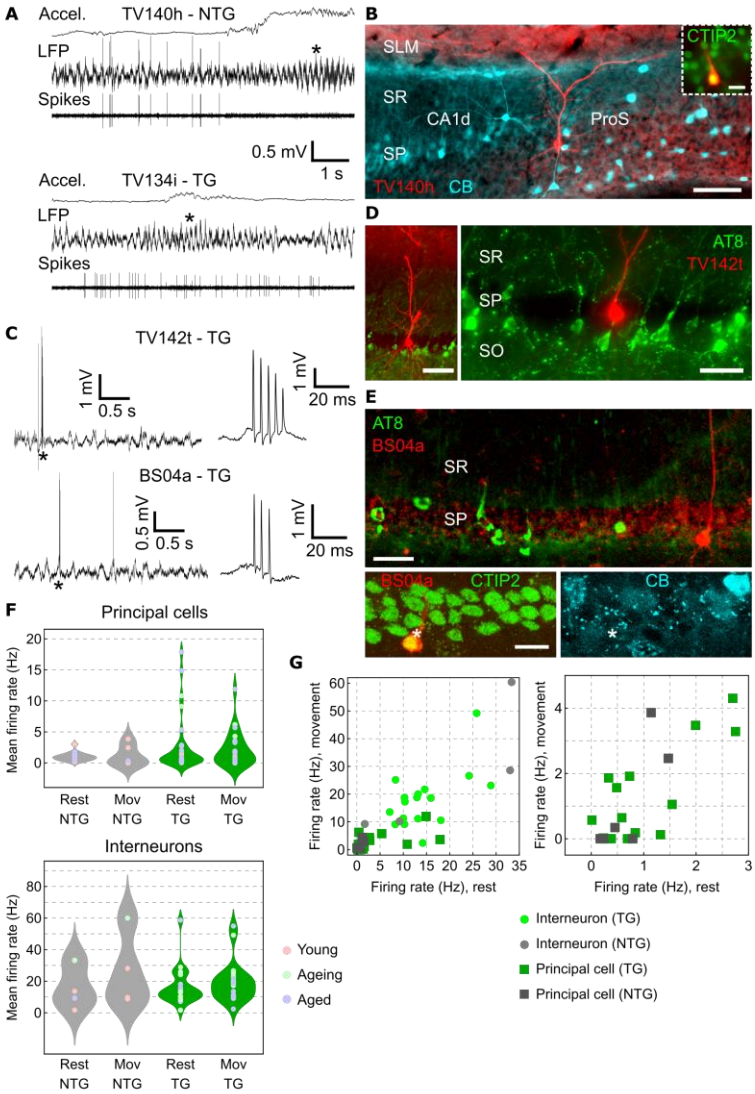

Figure 6. Identification of hippocampal neurons in relation to pTau.
(A) Glass electrode extracellular recordings of pyramidal neurons in freely moving mice. Top, ProS LFP and associated band-pass filtered spikes from cell TV140h during spontaneous rest and exploration (18 mo ntg). Bottom, CA1d LFP (tungsten wire, contralateral) and spikes from cell TV134i (10 mo tg). Accel., acceleration. Asterisks, higher amplitude theta during movement. **(B)** Cell TV140h from A in ProS (neurobiotin, red) is CB– (cyan) and CTIP2+ (inset, green). Widefield epifluorescence. **(C)** Glass electrode recordings in head-fixed tg mice. Wideband LFP of large irregular activity and spikes during rest from cells TV142t (top, 18 mo) and BS04a (bottom, 13 mo). Right, CS at higher time resolution (asterisks). **(D)** Identified CA1 pyramidal cell TV142t (neurobiotin, red) from C lacks pTau (green). Widefield epifluorescence. **(E)** Identified CA1 pyramidal cell BS04a (neurobiotin, red) from C lacks pTau (green) and CB (cyan, asterisk) but is CTIP2+ (green, asterisk). Confocal maximum intensity z-projections (top, 48.5 µm thick; bottom, 9.25 µm thick). **(F)** Distribution charts of mean firing rates during rest and movement. Top, pyramidal neurons; bottom, interneurons; ntg, gray; tg,

green. Points are individual neurons color coded by age group. **(G)** Firing rates for movement versus rest. Right, detail of lower firing cells from left. Scale bars (µm): B, D (left), 100; D (right), 50; E (top), 30; E (bottom), 15.

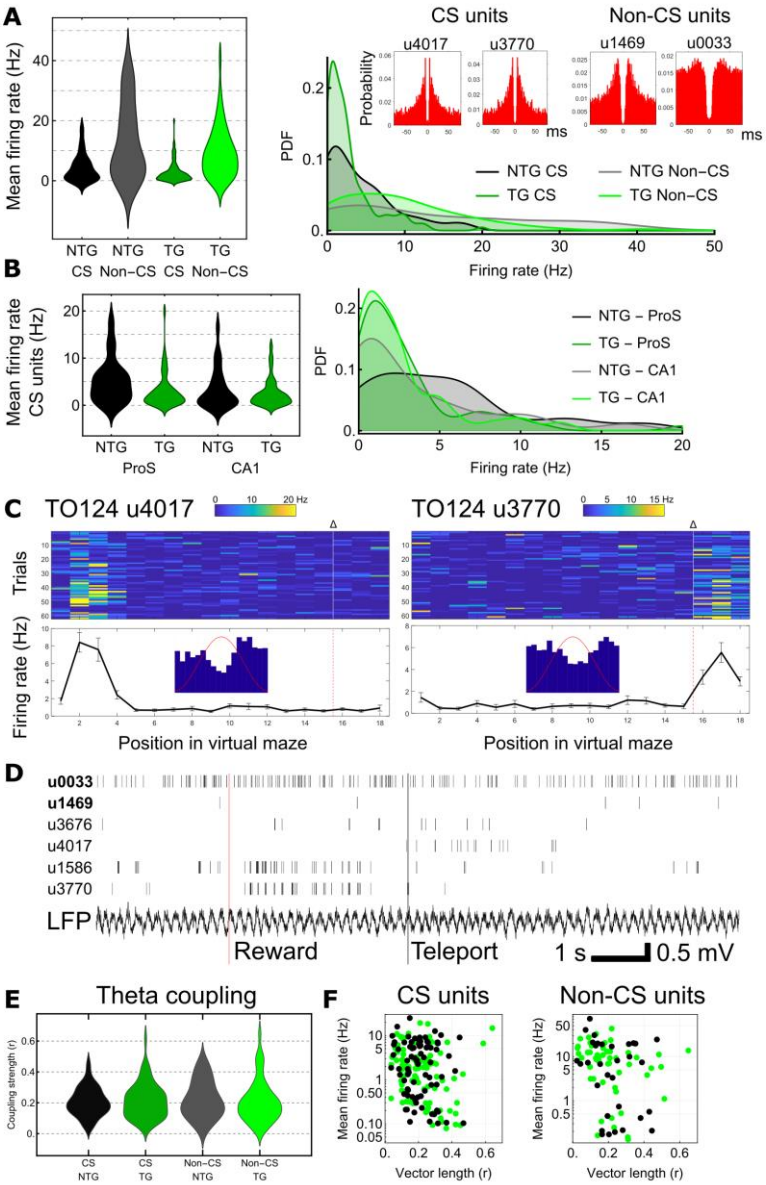

Figure 7. Loss of higher firing complex spiking cells but normal theta coupling in aged tg mice.

(A) Left, distribution charts of complex spiking (CS) and non-CS units for ntg and tg mice (pooled data; one high-firing outlier removed from the ntg non-CS group). Right, probability density function (PDF). Red autocorrelograms feature units from a tg mouse (case TO124, 23 mo). **(B)** As in A but separated by region (ProS/SUB and CA1) for CS units only. **(C)** Two place cells from case TO124: unit (u) 4017 most active towards start of virtual linear track, whereas u3770 most active following reward (Δ) at end of track. Color bars, 1 to 99 % of linearized firing rate (blue min., red max.). Insets, theta phase histogram (20° bins; 180° corresponds to peak shown by red sinusoid). **(D)** Spike trains from 6 units (case TO124); non-CS units in bold. Note u1586 and u3770 are rhythmically synchronized after reward.

'Teleport', re-initialization of linear track (new trial). Also note coupling to LFP theta cycles, and spikes corresponding to place field of u4017 from C. **(E)** Distribution chart of coupling strength (vector length, r) for all units. **(F)** Firing rate during theta versus vector length for individual units. Black, ntg mice; green, tg mice.

Methods

RESOURCE AVAILABILITY

Lead Contact

Further information and requests for resources and reagents should be directed to and will be fulfilled by the lead contact, Tim Viney (tim.viney@pharm.ox.ac.uk).

Materials Availability

This study did not generate new unique reagents.

Data and code availability

- Raw imaging and electrophysiological data reported in this paper will be shared by the Lead Contact upon request.
- All original code will be made publicly available as of the date of publication.
- Any additional information required to reanalyze the data reported in this paper is available from the lead contact upon request.

EXPERIMENTAL MODEL AND SUBJECT DETAILS

A total of 97 mice were used in this study (~50 % were female), comprising 51 heterozygous THY-Tau22 mice (tg), 43 non-transgenic littermates (ntg), and 3 C57Bl6j mice (wt). The THY-Tau22 transgenic mouse line was created by the group of Prof Luc Buée, with Thy1.2 driving expression of human *MAPT* with G272V and P301S mutations.[9] All animal procedures were approved by the local Animal Welfare and Ethical Review Body under approved personal and project licenses in accordance with the Animals (Scientific Procedures) Act, 1986 (UK) and associated regulations. We bred mice on a C57Bl6j background, as in the original publication. The oldest mouse was nearly 28 mo at the scientific endpoint (case TO117, tg female, glass electrode recordings; see below). Almost all aged mice reached their scientific end point (100 % of female ntg mice (n=16/16), 91 % of female tg mice (n=19/22), 94 % of male ntg mice (n=17/18), 100 % of male tg mice (n=13/13)).

Body weight was routinely monitored. Young male tg mice had reduced weight compared to ntg mice (~8 % difference; 31.6 ± 2.3 g ntg mice (n=11) and 26.8 ± 0.45 g tg mice (n=5); $F_{(1,14)}$ = 20.3, $p < 0.001$, one-way ANOVA; 3-5 mo; Fig. S2d), confirming previously published data [9]. Aged tg mice also had reduced body weight (38.3 ± 3.2 g male ntg (n=7), 28.8 ± 2.6 g male tg (n=7), 37.1 ± 0.77 g female ntg (n=4), 28 ± 1.4 g female tg (n=6); two-way ANOVA $F_{(1,20)}$ = 67.4, $P < 0.001$ for genotype, P = 0.7680 for sex, P = 0.7467 for genotype-sex interaction; 18-21 mo; Fig. S2d). In even older (22-25 mo) mice, there was a significant weight difference between sexes (37.5 ± 2.5 g male ntg (n=6), 27.3 ± 1.5 g male tg (n=6), 33.1 ± 6.9 g female ntg (n=8), 24.8 ± 2.9 h female tg (n=11); $F_{(1,27)}$ = 38.1, $P < 0.001$ for genotype, P = 0.0323 for sex, P = 0.5460 for genotype-sex interaction; Fig. S2d).

Of the 55 mice that underwent behavioral testing, 17 were subsequently implanted for electrophysiological recordings. A further 23 mice not tested behaviorally were also used for electrophysiological recordings. From this group, 3 aged tg mice (2 males, 1 female) had minor gait problems and tremor. Most mice were perfusion-fixed at their scientific endpoint, with

686 10/97 mice used only for histology. The remaining 8 mice were monitored for weight only
687 and not used in procedures. Animals were maintained in individually ventilated cages with
688 their littermates on a 12/12 h light-dark cycle (lights on at 07:00) and all behavioral tests were
689 carried out during the daytime. Implanted mice were also grouped housed wherever possible.
690 Room temperature was maintained at 21°C and humidity was between 50-60 %. Running
691 wheels were placed in the cages of mice undergoing habituation/training to the jet ball (see
692 below). All mice were fed on a standard RM3 diet (pellets, product 801700, Special Diets
693 Services). Each animal was assigned a name (two letters followed by a code, e.g. **TT**21D,
694 **TV**140), glass electrode recorded cells were assigned a lower case letter (e.g. TV140**h**, Fig. 6a),
695 and units isolated from silicon probes were assigned a code (e.g. TO124 u4017, Fig. 7c).

696 **METHOD DETAILS**

697 Electrophysiological recordings, behavioral tests, and cell counts were made blind to
698 genotype.

699 **Surgical procedures.**

700 Mice were anesthetized with isoflurane and the scalp was clipped. After subcutaneous
701 injection of Buprenorphine (0.1 mg/kg dose, Vetergesic, Ceva), mice were fixed to a
702 stereotaxic frame (Kopf Instruments) via ear bars and a jaw bar and maintained with 1–3 %
703 (v/v) isoflurane on a homeothermic blanket (Harvard Apparatus). Ocular lubricant was
704 applied to the eyes, and Bupivacaine (Marcaine, Aspen) was injected into the scalp. Under
705 aseptic conditions, an incision was made along the scalp to expose the skull. Two M1 screws
706 (Precision Technology Supplies) were fixed into the skull above the cerebellum, with one or
707 both used as electrical reference. Another screw was fixed ~1.50 mm anterior of the bregma.
708 After scoring the skull and applying a thin layer of cyanoacrylate super glue, a machined
709 glass-reinforced plastic D-shaped head plate (custom made at the Department of Physics,
710 Oxford University) was positioned over the screws and Refobacin bone cement (Zimmer
711 Biomet) was used to secure the head plate and screws to the skull. A 0.7 g head plate was used
712 for *head-fixed* and *freely moving mice*, and a slightly longer 1.1 g head plate was used for *jet ball*
713 experiments. Mice that failed to learn for jet ball experiments could be used in head-fixed
714 recordings. Similarly, if freely moving mouse recordings failed, head-fixed recordings could
715 be carried out instead. For the experiments involving freely moving mice, a 7 stranded
716 PerFluoroAlkoxy-coated steel wire (0.002 inch thickness, A-M Systems) was stereotaxically
717 inserted into CA1d to target stratum pyramidale (-2.30 mm antero-posterior (AP) and 1.50
718 mm medio-lateral (ML) from bregma, 1 mm below the dura mater) and secured with bone
719 cement and/or blue-light curing dental cement (Tetric EvoFlow, Ivoclar Vivadent). A custom-
720 made stainless steel NanoMotor holder (Department of Pharmacology, Oxford University)
721 was secured with bone cement to one side of the head plate. A headstage connector (a double
722 row of pins) was also secured to the head plate, and the tungsten wire and reference were
723 soldered to specific pins of the connector. Mice were administered a subcutaneous injection
724 of 0.5 ml 5 % (w/v) glucose in saline (Aqupharm 3, Animalcare) peri-operatively. Craniotomy
725 sites were as follows (mm from bregma): -2.90 AP, 1.75 ML (distal CA1d / proximal SUBd,
726 also known as prosubiculum [11,12], for the majority of mice); -3.20 AP, 1.90 ML (SUBd); -2.50
727 AP, 1.70 ML, 10° posterio-anterior angle (CA1d). In some mice, craniotomies were performed
728 during the first surgery immediately after head plate implantation. In all others (including all
729 mice for jet ball experiments), craniotomy sites were marked by partially drilling into the
730 skull, silicon (Smooth-On) was used to cover the skull inside the head plate, and mice were
731 left to recover in a home cage over a heated blanket. After habituation/training (below), a

732 second brief surgery was carried out, with the same anesthesia regime as above. Craniotomies
733 were performed at the marked sites, and the dura was removed with a bent 27 gauge needle.
734 Silicon was used to protect craniotomy sites and mice were left to recover in a home cage over
735 a heated blanket. Electrophysiology experiments were initiated the following day.

736 **Electrophysiology.**
737 *Glass electrode recordings in head-fixed mice.* Implanted mice were habituated to head-fixation
738 using a custom-made stainless steel block (Department of Physics, Oxford University),
739 secured to a heavy-duty frame (model 1430, Kopf Instruments). Mice could spontaneously
740 run and rest on a 30 cm diameter plastic Frisbee ('running disc') covered with paper roll. On
741 recording days, the silicon was removed and replaced with sterile saline. Two separate glass
742 electrodes filled with 3 % neurobiotin (w/v) in 0.5 M NaCl (8–18 MΩ) were advanced into the
743 craniotomy sites using IVM-1000 micromanipulators (Scientifica Ltd) to reach the
744 hippocampus/subiculum bilaterally. Signals were amplified x1000 (ELC-01MX, BF-48DGX
745 and DPA-2FS modules; npi Electronic GmbH, Tamm, Germany). Both wide-band (0.3 Hz to 8
746 kHz) and band-pass-filtered (action potentials, 0.8–8 kHz) signals were acquired in parallel
747 for each glass electrode and digitized at 20 kHz (Power1401; Cambridge Electronic Design
748 Ltd, Cambridge, UK). HumBugs (Digitimer Ltd) were used to remove 50 Hz noise. A video
749 camera was used to monitor behavior. Speed was measured using a rotary encoder (HEDM-
750 5500#B13, Avago Technologies) attached to the underside of the Frisbee. Data were recorded
751 using Spike2 software (Cambridge Electronic Design). Local field potential (LFP)
752 measurements and extracellular recordings of single neurons were made bilaterally during
753 spontaneous movement and rest periods. Cells of interest were juxtacellularly labeled with
754 200 ms positive current pulses, followed by a recovery period of at least 4 h.

755 *Glass electrode recordings in freely moving mice.* Mice were head-fixed as above and the
756 craniotomy site was exposed (the contralateral site had the implanted tungsten wire). A
757 custom-made piezo-electric NanoMotor (Kleindiek Nanotechnik and npi Electronic) was
758 secured in the holder on the head plate and a miniature preamplifier/headstage (custom-
759 made by npi Electronic) was attached to the headstage connector. A glass electrode containing
760 3 % neurobiotin in 0.5 M NaCl was attached to the NanoMotor and lowered into the brain.
761 The mouse was released from head restraint and placed in a 50 cm^2 open field with 30 cm high
762 walls. Occasionally objects were added to the environment. Acceleration was measured with
763 a built-in accelerometer and motion was tracked with a video camera and integrated LEDs on
764 the headstage or by body-motion capture. Extracellular single neuron recordings and LFP
765 measurements were made as for head-fixed mice, followed by juxtacellular labeling. Mice
766 were returned to head-fixation in order to remove the NanoMotor and miniature headstage
767 or continue head-fixed recordings as above.

768 *Jet ball recordings*. Mice were first handled for at least 2 d then *ad libitum* access to water was
769 removed to initiate water restriction. Mice were gradually habituated to head-fixation over an
770 air-suspended Styrofoam jet ball (part of a virtual reality setup, PhenoSys GmbH, Berlin,
771 Germany). Mice were trained to run on the jet ball to advance a virtual linear track (projected
772 in a dome). Once they reached the end, licking would release a 10 µl water reward (defining
773 the end of a trial). Animals were teleported to the start of the virtual corridor to initiate the
774 next run. Running followed by licking at the reward location was defined as goal-directed
775 navigation. Each animal was trained twice daily for ~30 min for 8-20 d. Throughout the
776 training days, the length of the virtual corridor was increased stepwise to make sure animals

were motivated to run to receive the reward. The reward tube was adjusted before each session to ensure animals could reach the water droplets upon delivery. Mice were closely monitored to receive at least 1 mL of water each day to avoid the weight dropping below 10 % of their initial body weight. At least one day per week animals received *ad libitum* water; food was always available. The day after the craniotomy, and on subsequent recording days, an acute 16-channel silicon probe (Buzsaki16-A16 probe, A1x16 linear probe or a A2x2 tetrode probe, NeuroNexus) was painted with DiI or DiO, connected to an RA16-AC preamplifier (Tucker-Davis Technologies) and gradually lowered into the hippocampal formation (Table S1). Up to 4 recording sessions were carried out per day (one hemisphere per session). The hippocampus was identified based on approximate depth, high power theta oscillations during running, sharp waves during rest, polarity of theta and sharp waves across the different channels, and the presence of high firing neurons in an ~100 μm band corresponding to stratum pyramidale. Signals were amplified x1000 (Lynx-8 amplifiers, Neuralynx), band-pass filtered (0.5 Hz to 8 kHz), digitized at 20 kHz with a Power1401 and recorded with Spike2. Jet ball movement, position along the virtual track, a lick sensor and reward delivery were synchronized to the recordings. A video camera was used to monitored behavior. Four implanted mice failed to learn goal-directed navigation (cases: TV147, female, ntg, 23 mo; TV148, female, ntg, 23 mo; TV164, male, tg, 17 mo; TV166, female, tg 19 mo) due to poor hindlimb gait and/or tremor. Instead, they were used for head-fixed recordings as above. One other implanted mouse had poor balance (case TV169, female, tg, 17 mo) and could not be trained or used for head-fixed recordings so was excluded. Silicon probe recording sites were confirmed by examining DiI/DiO fluorescence in serially processed brain sections.

Data analysis.

Data were analyzed in Mathematica (Wolfram Research), Python, MATLAB (The MathWorks), and Spike2.

Local field potentials (LFPs): In Spike2, DC shifts were removed with 0.3 s sliding windows then channels were downsampled to 1.25 kHz. Channels were either exported for analysis with other programs, or analyzed further in Spike2. Theta epochs were defined by the power ratio of theta (5-12 Hz) over delta (2-4 Hz) in 2 s windows (root mean square (rms) amplitude) being greater than 2. To calculate the peak theta frequency, LFPs recorded with glass electrodes were sampled at different depths of CA1d, predominantly from stratum pyramidale. Up to 5 theta epochs were sampled per recording, ranging from 4 to 34 s to define each epoch. A Hanning window (FFT size 2048, 0.6 Hz resolution) was used to compute the power spectral density in Spike2. The theta peak frequency was measured directly from the curve (interpolated with a cubic spline). Values obtained from 2-4 recordings per mouse were binned and averaged for low running speeds (4-6 cm/s) and 'high' speeds (6-10 cm/s). We also measured the theta peak from 6 mice (3 ntg, 3 tg) running in virtual reality; 3 theta epochs were randomly sampled from 1 recording per mouse from a representative channel of an acute silicon probe targeted to distal CA1d. Theta epochs were between 10 and 218 s (mean of 94 ± 61 s). Actual speed could not be determined for these recordings. Ripples (band-pass filtered, 130-230 Hz) were detected from glass electrode LFP recordings by selecting periods where the rms amplitude (power) was greater than 3 standard deviations above the mean power. At least 2 recordings were sampled per animal, ranging from 31 to 94 detected ripples.

Hilbert-Huang transform.[83] Empirical mode decomposition (EMD) was carried out in Python using the emd package (https://gitlab.com/emd-dev/emd) and its dependencies.[40] Sampled

822 glass electrode recordings ranged from 14 to 100 s of unfiltered LFP containing mostly
823 movement periods. For silicon probe recordings, sampled LFPs containing running periods
824 on the jet ball ranged from 57 to 182 s. To obtain intrinsic mode functions (IMFs), the following
825 masks were used for masked EMD (emd.sift.mask_sift): (350, 200, 70, 40, 30, 7, 1) divided by
826 the sampling rate. Instantaneous amplitude, frequency and phase were obtained for each IMF
827 using emd.spectra.frequency_transform with the Normalized-Hilbert Transform (nht). We
828 excluded IMF1 as it contained mostly noise, and excluded any mid-gamma range IMF that
829 had 50 Hz electrical noise or poor movement periods (low signal to noise ratio). Consequently,
830 1 ntg and 1 tg mouse were excluded for IMF3. Phase amplitude coupling was analyzed using
831 emd.spectra.hilberthuang, binning the theta IMF instantaneous phase values. We excluded 1
832 aged tg and 1 ntg mouse due to 50 Hz electrical noise. We also excluded 1 ntg mouse that
833 lacked sufficient movement for PAC detection, and another ntg mouse due to the glass
834 electrode positioned within stratum radiatum.

835 *Single neuron glass electrode recordings*. Recording locations were estimated from at least two of
836 the following features: relative depth from a juxtacellularly-labelled recovered cell on the
837 same pipette tract; LFP profile (e.g. positive sharp waves (deep layers) or negative going sharp
838 waves (superficial layers), presence of ripples (highest amplitude in pyramidal cel layers),
839 shape and amplitude of theta oscillations, cross frequency coupling of mid-gamma
840 oscillations to the peak of theta cycles (CA1 stratum pyramidale), presence or absence of
841 'dentate spikes' for the dentate gyrus); evidence of a pipette tract and/or a cluster of weakly-
842 labeled cells marking a recording location. Unlabeled/non-recovered prinicipal cells were
843 compared to recovered (labeled) cells based on the presence or absence of complex spike
844 bursts. Only data acquired before juxtacellular labeling were used for analysis. For firing rates,
845 spikes within a complex spike (CS) burst were counted individually.

846 *Acute silicon probe recordings.* Spikes were detected, sorted, and clustered offline using
847 Kilosort2.[84] Subsequently, interactive visualization and manual curation of the data were
848 carried out using phy software [85] in order to obtain well-isolated and stable units based on
849 refractory periods, spike waveform and cross-correlations.[38] Units with firing rates < 0.1 Hz
850 were excluded from further analysis. The first trial from each session and any trials showing
851 electrode drift were excluded. Data analyses were performed using built-in or custom-written
852 software in MATLAB and Spike2. Firing rates (spikes/s) were computed across 18 sequential
853 bins: We split each run into 15 spatial bins covering the virtual corridor followed by 3 temporal
854 bins (1 s each) covering the end of the corridor corresponding to the reward location (the
855 virtual environment was locked for 3 seconds when mice reached the end of the corridor in
856 order to receive the water reward). Units were classified as complex spike (CS) cells if they
857 showed a prominent peak between 3-8 ms in their spike time autocorrelograms followed by
858 a relatively fast decay.[38,47] Units were compared to a separate dataset from,[43] who defined
859 putative pyramidal cells (PCs, Table S1) as units with "an overall firing rate < 3 Hz, a spike
860 width at 90% of the peak amplitude above 0.5 ms, and an event autocorrelogram value below
861 10 ms". For firing rate analysis, one session each was excluded for animals TV149 and TO125
862 due to probes being located in the isocortex, just dorsal of the hippocampus (6 units in total),
863 and one session was excluded for animal TV179 due to a lack of isolated units.

864 *Place cell classification.* Significant peak firing rates along the virtual corridor were computed
865 by a permutation test as described by Ozdemir et al.[86] Each unit's firing rate was calculated
866 across 18 spatio-temporal bins. Then, we randomly shuffled these time windows within a run

867 for every trial, calculating a surrogate firing rate. Upon repeating this procedure 10,000 times,
868 we obtained the *P* values of spatial firing modulation by comparing the actual firing rate to
869 the distribution of surrogate rates. Subsequently, significance limits were corrected using a
870 false discovery rate method for multiple comparisons. Well-isolated units were deemed place
871 cells if they had a significantly higher firing rate in at least one spatial bin along the virtual
872 corridor.

873 *Theta coupling.* A representative silicon probe site was selected for theta coupling analysis
874 based on the profile of the unfiltered LFP, the extrapolated position from the recovered probe
875 site (DiO or DiI tract), and the probe map. Mostly positive deflections in the LFP during non-
876 running periods and typically high power theta oscillations during running indicated a likely
877 stratum pyramidale or stratum oriens location. After detecting theta epochs as for glass
878 electrode recordings above, theta phase was calculated by linear interpolation between
879 troughs of the band-pass-filtered (5-12 Hz) theta oscillations, with 0° and 360° set as the
880 troughs. The Rayleigh test was used to test for uniformity of circular phase distributions; the
881 mean phase and mean vector length (r) were used as measures of the preferred phase and
882 coupling strength, respectively (using custom scripts written in Mathematica). For ntg mice,
883 we sampled 968-1,745 s duration theta periods (72,523 theta cycles) and excluded CS units and
884 non-CS units that had fewer than 72 and 241 spikes, respectively. For tg mice, we sampled
885 291-3,023 s duration theta periods (91,233 theta cycles) and excluded CS cells and non-CS cells
886 with fewer than 45 and 168 spikes, respectively.

887 **Behavioral tasks.**
888 *Spatial novelty preference Y-maze task*. This task was designed to assess short-term spatial
889 memory with the expectation that normal mice prefer novel over familiar spatial
890 environments.[26,75] A solid black plastic Y-maze (30 cm arms, 7 cm wide, 20 cm high walls) was
891 positioned 17 cm from the floor. There were no intra-maze cues except for a 20 cm high
892 magenta block that blocked one of the arms. Prominent extra-maze cues were used. One arm
893 was designated as the 'novel arm', another the 'start arm', and the third as the 'other arm'.
894 The novel arm was blocked off and the mouse was placed in the start arm and was able to
895 freely explore the start and other arms (exposure phase). After 5 minutes, the block was
896 removed and mice could explore all 3 arms (test phase). Each mouse was only tested once,
897 and arm assignment was counterbalanced for genotype and cohort. The maze was cleaned
898 with ethanol before each test. Time spent in each arm was calculated manually or using
899 ezTrack;[87] total distance traveled (path length) was calculated using ezTrack. We excluded 3
900 mice from the path length analysis due to obstructions in the videos.

901 *Water escape Y-maze task*. This task was used to assess spatial reference memory without the
902 confound of anxiety-related thigmotaxis, which is sometimes evident in the open field water
903 maze.[29-31] An enclosed Y-maze made of clear Perspex (30 cm arms, 8 cm wide, 20 cm high
904 walls) was filled with water made opaque by mixing in white 'ready mix paint' (Reeves). A
905 hidden inverted glass beaker (~6 cm diameter) was kept submerged at the end of one of the
906 arms ('goal arm'). Extra-maze cues were kept constant. At the start of each trial, the mouse
907 was placed in one of the other two arms ('start arms'). The start arm was allocated
908 pseudorandomly across trials for each mouse with no more than 2 consecutive starts from the
909 same arm and equal numbers of starts from the arm to the left and right of the target arm in
910 each block of trials). The goal arm remained the same for each animal, but the allocation of
911 the goal arm was counterbalanced for genotype and cohort. The mouse was allowed to swim

freely until it reached the hidden platform. However, if it did not reach the platform by 90 s it was guided by the experimenter. The mouse was allowed to remain on the platform for 30 s before being removed. There were 5 trials/d for 10 days (acquisition training) with an inter-trial interval of 15 s. For each trial, the first arm entered (choice) was scored 1 for the goal arm and 0 for the other arm or re-entered the start arm. A block was defined as 5 trials, with performance expressed as percentage of correct first choices (choice accuracy). On day 11, a probe trial was performed, whereby the platform was removed and the mouse was allowed to swim freely for 60 s. One ntg mouse was excluded from analysis as it failed to make choices on days 4-10.

Non-matching to place T-maze task (rewarded alternation). This task assessed spatial working memory.[32] The T maze consisted of a 50 x 10 cm start arm and two identical 30 x 10 cm goal arms. Walls were 10 cm high, and the maze was raised 44 cm off the floor. Group-housed mice were maintained on a restricted feeding schedule to ~90 % of their free-feeding weight and fed every day at 16:00. On the 6th day after starting food restriction, mice were habituated to 50% sweetened condensed milk in a dish in their home cage in the holding room. The next day, milk was provided in their cages inside the behavior-testing room (context 1). The following day, cagemates were group habituated to the T-maze with 0.5 ml milk rewards in plastic dishes at the ends of both goal arms. The room was well-lit and contained extra-maze cues. An odorless cleaning solution was used to clean the maze before testing different cages. After several more days on food restriction, non-matching to place testing began. Each trial consisted of a 'forced run' and a 'choice run', with 4 trials per day defined as a session. In the forced run, one goal arm was blocked with a wooden block. Mice were placed into a blocked-off start box at the far end of the start arm. After this start block was removed, mice had to run to the unblocked goal arm for a 0.1 ml reward. The blocked goal arm was determined by a pseudorandom sequence (with equal numbers of left and right turns per session, with no more than 2 consecutive turns in the same direction). If the mouse did not initiate a run within 60 s after removing the start black, the mouse would be re-tested after all the other cagemates were tested in that session. For all trials, the delay time in task initiation was measured from start block removal until leaving the start box area. After sampling the reward on the forced run, the mouse was removed from the maze. The mouse was placed back at the far end of the start arm and now had to choose between the goal arms (now with both arms unblocked). The average time between sampling the reward on the forced run to being free to initiate the choice run from the far end of the start arm was 16 s (from n=3,240 trials). The mouse was rewarded for choosing the unvisited (previously blocked) arm, i.e. for alternating. An alternation score was calculated by scoring 1 for alternating and 0 for not alternating. Mice were tested one trial at a time, so that all cagemates were tested once before starting their second trial (~4-8 min inter-trial interval, depending on cage size). A total of 10 sessions were undertaken for each mouse (40 trials total), and analyzed as blocks of 4 trials. The same mice were tested at 3 different ages, with the 2nd and 3rd tests no requiring habituation. Since ntg and tg mice reached high levels of performance (see Results), differences between genotypes might be revealed by using an unfamiliar context. In context 2, a different testing room was used featuring different extra-maze cues, an R-Carvone odor, and prominent intra-maze cues (white stripes on the maze floor and a red cross on the block), and cleaning was carried out with ethanol instead of the odorless cleaning solution.

Elevated plus maze. To test anxiety-related behavior, mice familiar to other behavioral tasks were placed individually in the center of an elevated plus maze facing an open arm. Two

958 versions were used: one had 36 x 7 cm open and closed arms, 21.5 cm high gray wooden walls
959 for the closed arms, and positioned 69 cm from the floor (for 3 mo mice). The other had 32 x 9
960 cm arms, 19.5 cm high black plastic walls for the closed arms, and was 92 cm from the floor
961 (for 12 mo mice). The time spent in open and closed arms was measured over 5 min, excluding
962 the junction.

963 **Histology and imaging.**
964 *Tissue processing.* Mice were deeply anesthetized with sodium pentobarbital (50 mg/kg, i.p.)
965 and transcardially perfused with saline followed by 4% paraformaldehyde, 15% v/v saturated
966 picric acid, and 0.05% glutaraldehyde in 0.1 M phosphate buffer (PB), pH 7.4. Some brains
967 were post-fixed overnight in fixative lacking the glutaraldehyde. After washing in 0.1 M PB,
968 70 µm coronal sections were cut using a Leica Microsystems VT 1000S vibratome and stored
969 in 0.1 M PB with 0.05% sodium azide at 4°C. To visualize neurobiotin-labeled neuronal
970 processes, tissue sections were permeabilized in Tris-buffered saline (0.9% NaCl buffered with
971 50 mM Tris, pH 7.4; TBS) with 0.3% Triton X-100 (TBS-Tx) or through rapid 2x freeze–thaw
972 (FT) over liquid nitrogen (cryoprotected in 20% sucrose in 0.1 M PB) then streptavidin-
973 conjugated Alexa Fluor 488 was applied at 1:1000 dilution in TBS-Tx (or TBS if permeabilized
974 with FT) for 4 h at room temperature (RT) or overnight at 4°C. Sections were washed in
975 TBS/TBS-Tx and mounted to slides in Vectashield (Vector Laboratories).

976 *Immunohistochemistry.* Sections were blocked for 1 h in 20 % normal horse serum (NHS) in
977 TBS/TBS-Tx followed by 3 d incubation at 4°C in primary antibody solution containing 1 %
978 NHS in TBS/TBS-Tx. The following primary antibodies (and dilutions) were used: Mouse
979 anti-AT8 1:5000 (MN1020, lot ND 169248, Thermo Fisher Scientific; this antibody specifically
980 recognizes Tau phosphorylated at serine 202 and threonine 205 residues of human Tau [88]),
981 goat anti-Calbindin 1:500 (Calbindin-Go-Af1040, Frontier Institute), rabbit anti-Calbindin
982 1:5000 (CB-38, lot No.5.5, Swant), rabbit anti-Calretinin 1:1000 (7699/3H, lot 18299, Swant),
983 rabbit anti-Ctip2 1:1000 (25B6, ab18465, Abcam), rabbit anti-Olig2 1:500 (AB9610, lot
984 0603024913, Millipore), guinea pig anti-Parvalbumin 1:250 (195004/1-19, Synaptic Systems),
985 rabbit anti-Parvalbumin (PV 27, lot 2014, Swant), rabbit anti-PCP4 1:1000 (sc-293258, lot
986 GO814, Santa Cruz), goat-anti Satb1 1:250 (N-14, sc-5989, Santa Cruz), rabbit anti-Satb2 1:1000
987 (ab34735 and ab92446, Abcam), chicken anti-Tyrosine hydroxylase 1:500 (ab76442, Abcam),
988 rabbit anti-Wfs1 1:1000 (11558-1-AP, lot 00043335, Proteintech). Specificity references can be
989 found in the following publications: [63,64,89,90]. Sections were washed 3 times in TBS/TBS-Tx
990 then incubated in secondary antibody solution containing 1 % NHS in TBS/TBS-Tx for 4 h RT
991 or overnight at 4°C. The following secondary antibodies (and dilutions) were used in various
992 combinations (all raised in donkey): 1:250 anti-guinea pig and anti-rabbit DyLight 405 1:250
993 (706-475-148), anti-rabbit Violet421 1:100-200 (713-675-152, 705-605-147, 711-475-152), anti-
994 mouse and anti-rabbit Alexa Fluor 488 1:1000 (711-605-152, 711-545-152), anti-rabbit and anti-
995 chicken Cy3 1:400 (711-165-152, 703-165-155), anti-goat Cy5 1:250 (705-605-147), anti-goat Cy5
996 1:250 (705-605-147), anti-guinea pig and anti-rabbit Alexa Fluor 647 1:250 (706-475-148, 711-
997 605-152) from Jackson ImmunoResearch and Alexa Fluor 405 (A31556) from Invitrogen. After
998 3 washes, sections were mounted in Vectashield.

999 *Fluorescence microscopy.* Sections were visualized and imaged with widefield epifluorescence
1000 using a Leitz DMRB microscope (Leica Microsystems) equipped with PL Fluotar objectives
1001 (magnification/numerical aperture: 5x/0.15, 10x/0.3, 20x/0.5, 40x/0.7; OpenLab software) or
1002 an AXIO Observer Z1 microscope (LSM 710; Zeiss) equipped with Plan-Apochromat 10x/0.3,

1003 20x/0.8 and 40x/1.4 objectives (Axiovision or ZEN Blue 2.6 software). For confocal
1004 microscopy, the LSM 710 was used with Plan-Apochromat 40x/1.4, 63x/1.4, and 100x/1.46
1005 objectives (ZEN 2008 5.0 or ZEN Black 14.0 software). Laser lines (solid-state 405 nm, argon
1006 488 nm, HeNe 543 nm and HeNe 633nm) were configured with the appropriate beamsplitters.
1007 The pinhole was set to ~1 Airy Unit for each channel.

1008 *Fluorescence measurements and cell counts.* To measure the intensity of AT8 immunoreactivity
1009 (Fig. 1b), 10x magnification epifluorescence tiles were made of the hippocampal formation.
1010 Three 300 μm^2 regions of interest (ROIs) were selected, covering the ProS and two regions of
1011 CA1d. The mean pixel intensity was normalized relative to a background ROI. At least 2 mice
1012 per age group were measured. For quantification of CB and pTau colocalization, we examined
1013 pTau+ somata within the pyramidal cell layer, randomly sampling ~20 (range 7-28) pTau+
1014 cells per case for 3-5 cases per age group. To count the number of CA1 pyramidal cells in age-
1015 matched ntg and tg mice (Fig. 2H), we imaged SATB2 immunopositive or DAPI stained nuclei
1016 with a 20x/0.5 lens focused on the top of 70 µm-thick coronal sections containing CA1d
1017 starting from proximal CA1 adjacent to the SATB2 immunonegative CA2 region. Counting
1018 was carried out using the Cell Counter plugin in Fiji (ImageJ). We averaged counts from 3
1019 hemispheres per mouse, then compared the resulting mean counts from 2-3 mice per
1020 genotype. All quantifications were blind to genotype and age.

1021 *Single- and double-labeling pre-embedding immunohistochemistry and electron microscopy*. Floating
1022 sections from cases TT21D (22.5 mo female) and TT33G (21.5 mo female) were washed 3x in
1023 TBS and blocked in 5% normal goat serum (NGS) in TBS for 45 min. Next, sections were
1024 incubated with AT8 and/or Olig2 primary antibodies in TBS for 6 d at 4°C. The following
1025 immunoreactions were performed: (1) One primary antibody with immunogold labelling
1026 followed by silver intensification; (2) one primary antibody with peroxidase reaction; (3) two
1027 primary antibodies, visualized by a silver-intensified immunogold reaction, followed by an
1028 immunoperoxidase reaction; (4) control, no primary antibody, immunogold and biotinylated
1029 secondary antibodies followed by silver-intensification. After incubation with primary
1030 antibodies, sections were rinsed three times in TBS and blocked for 30 min at RT in 0.1 % Cold
1031 Water Fish Skin Gelatin (CWFS) solution containing 0.8% NGS and 0.05% sodium azide in
1032 TBS to reduce non-specific background reactions. Next, sections were incubated overnight at
1033 4°C in 1:300 biotinylated goat anti-rabbit IgG (Vector Labs, BA-1000) and 1:200 donkey anti-
1034 mouse ultrasmall immunogold (Aurion, 100.322) in CWFS solution. Sections were washed
1035 several times in TBS and once in 0.1 M PB followed by incubation with 2% glutaraldehyde in
1036 PB to fix the antibodies conjugated to immunogold particles. After repeated washes in TBS,
1037 sections were incubated overnight at 4°C in avidin-biotinylated horseradish peroxidase
1038 complex (Vectastain ABC Elite kit, Vector Laboratories) in TBS. To visualize immunogold
1039 particles, they were intensified with silver: first the sections were treated with enhancement
1040 conditioning solution (ECS; Aurion) diluted 10x with distilled water for 3x5 min. To enlarge
1041 the gold particles further, sections were then incubated in silver enhancement solution (SE-
1042 LM, Aurion) for 20 min at 20°C and washed in ECS. Subsequently, peroxidase was visualized
1043 using 3,3-diaminobenzidine (DAB; 0.5 mg/ml, Sigma-Aldrich) as chromogen developed with
1044 0.01% H_2O_2. The same method and reagents were used for single and double labeling. After
1045 washing sections in PB, they were treated with 0.5% OsO_4 (a fixative and heavy metal
1046 contrasting agent) in 0.1 M PB for 20 min on ice to control reaction time. Next, dehydration of
1047 sections was carried out in ascending ethanol series (50%, 70%, 90%, 95%, 100%) and in
1048 acetonitrile. To enhance contrast for electron microscopy, sections were incubated in 1 %

uranyl acetate diluted in 70% ethanol for 25 min between the 70% and 90% ethanol steps. Subsequently, sections were placed in epoxy resin (Durpucan AMC, Fluka, Sigma-Aldrich), incubated overnight at RT and transferred onto slides. For polymerization, sections were incubated at 60°C for 2 d. Selected regions of proximal SUBd and/or distal CA1d were re-embedded into Durcupan blocks. A series of ~50 nm-thick sections were cut with an ultramicrotome (Leica Ultracut UTC) and collected on pioloform-coated copper grids. Finally, sections were counterstained with lead citrate and studied on a Jeol 1010 transmission electron microscope equipped with a digital GATAN Orius camera (Department of Physiology, Anatomy and Genetics, Oxford University).

QUANTIFICATION AND STATISTICAL ANALYSIS

Mean and standard deviation (s.d.) are reported as mean ± s.d.; median and interquartile range (IQR) are reported as median [IQR]. Experimental units (e.g. mice, cells) are specified in the text after the n values. Statistical analysis was carried out in Mathematica, GraphPad Prism, and SPSS (versions 25 and 28, IBM). The alpha was set to 0.05. For data that approximated a normal distribution, unpaired Student's T tests were used to compare two groups, otherwise Mann-Whitney tests were used. For comparisons of more than two groups we used Analysis of Variance (ANOVA) for parametric data. To account for variability in samples from different mice for silicon probe recording data (firing rates and vector lengths), we used a linear mixed model in SPSS with mouse as a random factor, and genotype, region and 'cell type' (CS, non-CS) as fixed factors. For analysis of circular data, we used the Rayleigh test (Z). The following test statistics are specified in the text and refer to the following tests: D, Kolmogorov-Smirnov; U, Mann-Whitney; t, unpaired T test; F, ANOVA.

REAGENT or RESOURCE	SOURCE	IDENTIFIER
Antibodies		
AT8	Thermo Fisher Scientific	MN1020, RRID: AB_223647
Calbindin	Frontier Institute	Calbindin-Go-Af1040, RRID: AB_2571569
Calbindin	Swant	CB-38, RRID: AB_10000340
Calretinin	Swant	7699/3H, RRID: AB_10000321
Ctip2	Abcam	ab18465, RRID: AB_2064130
Olig2	Millipore	AB9610, RRID: AB_570666
Parvalbumin	Synaptic Systems	195004/1-19, RRID: AB_2156476
Parvalbumin	Swant	PV 27, RRID: AB_2631173
PCP4	Santa Cruz	GO814
Satb1	Santa Cruz	sc-5989, RRID: AB_2184337
Satb2	Abcam	ab34735, RRID: AB_2301417
Satb2	Abcam	ab92446, RRID: AB_10563678
Tyrosine hydroxylase	Abcam	ab76442, RRID: AB_1524535
Wfs1	Proteintech	11558-1-AP, RRID: AB_2216046
Chemicals, peptides, and recombinant proteins		
Neurobiotin tracer	Vector Laboratories	#SP-1120; RRID: AB_2313575
Isoflurane inhalation anesthesia	Teva Ltd.	https://products.tevauk.com/p/Category?id=185
Vetergesic (0.3 mg/ml Buprenorphine)	Ceva	
Marcain (Bupivacaine)	Aspen	#PS09728
Refobacin bone cement	Zimmer Biomet	#3003940002-3
Tetric EvoFlow dental cement	Ivoclar Vivadent	A1
DiI tracer	Life Technologies	#V22889
DiO tracer	Life Technologies	#V22889
R-Carvone	Sigma-Aldrich	#124931

Normal horse serum	Vector Laboratories	S-2000
Normal goat serum	Vector Laboratories	S-1000
Cold Water Fish Skin Gelatin	Aurion	#900.033
Enhancement conditioning solution ECS	Aurion	Lot 01207/3
Silver enhancement solution SE-LM	Aurion	#500.022
Diaminobenzidine	Sigma-Aldrich	D5637-1G
Critical commercial assays		
Vectastain ABC Elite kit	Vector Laboratories	Cat# PK6100; RRID: AB_2336819
Vectashield Antifade Mounting Medium	Vector Laboratories	Cat# H-1000; RRID: AB_2336789
Experimental models: Organisms/strains		
C57BL6j mice	Charles River Laboratories	https://www.criver.com/
THY-Tau22 mice	Schindowski et al.[9]	http://www.informatics.jax.org/allele/MGI:3717232
Software and algorithms		
Fiji	ImageJ	https://imagej.net/software/fiji/
Mathematica	Wolfram Research	https://www.wolfram.com/mathematica/
MATLAB	Mathworks	www.mathworks.com/products/matlab.html
Zen 2008, Zen Black, Zen Blue, Axiovision	Zeiss	www.zeiss.co.uk
Spike2	Cambridge Electronic Design	http://ced.co.uk/
Kilosort2	Stringer et al.[84]	https://github.com/MouseLand/Kilosort
phy	Rossant et al.[85]	https://klusta.readthedocs.io/en/latest/
Python		https://www.python.org/
ezTrack	Pennington et al.[87]	https://github.com/denisecailab/ezTrack
EMD	Quinn et al.[40]	https://gitlab.com/emd-dev/emd

SPSS	IBM	https://www.ibm.com/products/spss-statistics
Prism 7	Prism 7 GraphPad	https://www.graphpad.com/
Other		
Buzsaki16-A16 silicon probe	NeuroNexus	https://neuronexus.com/
A1x16 linear silicon probe	NeuroNexus	https://neuronexus.com/
A2x2 tetrode silicon probe	NeuroNexus	https://neuronexus.com/

1071

References

1. Goedert, M., Eisenberg, D.S., and Crowther, R.A. (2017). Propagation of Tau Aggregates and Neurodegeneration. Annu Rev Neurosci *40*, 189-210. 10.1146/annurev-neuro-072116-031153.
2. Arakhamia, T., Lee, C.E., Carlomagno, Y., Duong, D.M., Kundinger, S.R., Wang, K., Williams, D., DeTure, M., Dickson, D.W., Cook, C.N., et al. (2020). Posttranslational Modifications Mediate the Structural Diversity of Tauopathy Strains. Cell *180*, 633-644 e612. 10.1016/j.cell.2020.01.027.
3. Wilson, R.S., Leurgans, S.E., Boyle, P.A., and Bennett, D.A. (2011). Cognitive decline in prodromal Alzheimer disease and mild cognitive impairment. Arch Neurol *68*, 351-356. 10.1001/archneurol.2011.31.
4. Moscoso, A., Silva-Rodriguez, J., Aldrey, J.M., Cortes, J., Fernandez-Ferreiro, A., Gomez-Lado, N., Ruibal, A., Aguiar, P., and Alzheimer's Disease Neuroimaging, I. (2019). Staging the cognitive continuum in prodromal Alzheimer's disease with episodic memory. Neurobiol Aging *84*, 1-8. 10.1016/j.neurobiolaging.2019.07.014.
5. Vogel, J.W., Iturria-Medina, Y., Strandberg, O.T., Smith, R., Levitis, E., Evans, A.C., Hansson, O., Alzheimer's Disease Neuroimaging, I., and Swedish BioFinder, S. (2020). Spread of pathological tau proteins through communicating neurons in human Alzheimer's disease. Nat Commun *11*, 2612. 10.1038/s41467-020-15701-2.
6. Lewis, J., McGowan, E., Rockwood, J., Melrose, H., Nacharaju, P., Van Slegtenhorst, M., Gwinn-Hardy, K., Paul Murphy, M., Baker, M., Yu, X., et al. (2000). Neurofibrillary tangles, amyotrophy and progressive motor disturbance in mice expressing mutant (P301L) tau protein. Nat Genet *25*, 402-405. 10.1038/78078.
7. Ramsden, M., Kotilinek, L., Forster, C., Paulson, J., McGowan, E., SantaCruz, K., Guimaraes, A., Yue, M., Lewis, J., Carlson, G., et al. (2005). Age-dependent neurofibrillary tangle formation, neuron loss, and memory impairment in a mouse model of human tauopathy (P301L). J Neurosci *25*, 10637-10647. 10.1523/JNEUROSCI.3279-05.2005.
8. Leroy, K., Bretteville, A., Schindowski, K., Gilissen, E., Authelet, M., De Decker, R., Yilmaz, Z., Buee, L., and Brion, J.P. (2007). Early axonopathy preceding neurofibrillary tangles in mutant tau transgenic mice. Am J Pathol *171*, 976-992. 10.2353/ajpath.2007.070345.
9. Schindowski, K., Bretteville, A., Leroy, K., Begard, S., Brion, J.P., Hamdane, M., and Buee, L. (2006). Alzheimer's disease-like tau neuropathology leads to memory deficits and loss of functional synapses in a novel mutated tau transgenic mouse without any motor deficits. Am J Pathol *169*, 599-616. 10.2353/ajpath.2006.060002.
10. Frederick, C., Ando, K., Leroy, K., Heraud, C., Suain, V., Buee, L., and Brion, J.P. (2015). Rapamycin ester analog CCI-779/Temsirolimus alleviates tau pathology and improves motor deficit in mutant tau transgenic mice. J Alzheimers Dis *44*, 1145-1156. 10.3233/JAD-142097.
11. Ding, S.L., Yao, Z., Hirokawa, K.E., Nguyen, T.N., Graybuck, L.T., Fong, O., Bohn, P., Ngo, K., Smith, K.A., Koch, C., et al. (2020). Distinct Transcriptomic Cell Types and Neural Circuits of the Subiculum and Prosubiculum along the Dorsal-Ventral Axis. Cell Rep *31*, 107648. 10.1016/j.celrep.2020.107648.
12. Lorente De Nó, R. (1934). Studies on the structure of the cerebral cortex. II. Continuation of the study of the ammonic system. Journal für Psychologie und Neurologie *46*, 113-177.
13. Van der Jeugd, A., Vermaercke, B., Derisbourg, M., Lo, A.C., Hamdane, M., Blum, D., Buee, L., and D'Hooge, R. (2013). Progressive age-related cognitive decline in tau mice. J Alzheimers Dis *37*, 777-788. 10.3233/JAD-130110.
14. Degiorgis, L., Karatas, M., Sourty, M., Faivre, E., Lamy, J., Noblet, V., Bienert, T., Reisert, M., von Elverfeldt, D., Buee, L., et al. (2020). Brain network remodelling reflects tau-related pathology prior to memory deficits in Thy-Tau22 mice. Brain *143*, 3748-3762. 10.1093/brain/awaa312.

1122 15. Lapray, D., Lasztoczi, B., Lagler, M., Viney, T.J., Katona, L., Valenti, O., Hartwich, K., Borhegyi,
1123 Z., Somogyi, P., and Klausberger, T. (2012). Behavior-dependent specialization of identified
1124 hippocampal interneurons. Nat Neurosci *15*, 1265-1271. 10.1038/nn.3176.
1125 16. Valero, M., Cid, E., Averkin, R.G., Aguilar, J., Sanchez-Aguilera, A., Viney, T.J., Gomez-
1126 Dominguez, D., Bellistri, E., and de la Prida, L.M. (2015). Determinants of different deep and
1127 superficial CA1 pyramidal cell dynamics during sharp-wave ripples. Nat Neurosci *18*, 1281-
1128 1290. 10.1038/nn.4074.
1129 17. Sakakibara, Y., Sekiya, M., Fujisaki, N., Quan, X., and Iijima, K.M. (2018). Knockdown of wfs1,
1130 a fly homolog of Wolfram syndrome 1, in the nervous system increases susceptibility to age-
1131 and stress-induced neuronal dysfunction and degeneration in Drosophila. PLoS Genet *14*,
1132 e1007196. 10.1371/journal.pgen.1007196.
1133 18. Chen, S., Acosta, D., Li, L., Liang, J., Chang, Y., Wang, C., Fitzgerald, J., Morrison, C.,
1134 Goulbourne, C.N., Nakano, Y., et al. (2022). Wolframin is a novel regulator of tau pathology
1135 and neurodegeneration. Acta Neuropathol *143*, 547-569. 10.1007/s00401-022-02417-4.
1136 19. Sanchez-Aguilera, A., Wheeler, D.W., Jurado-Parras, T., Valero, M., Nokia, M.S., Cid, E.,
1137 Fernandez-Lamo, I., Sutton, N., Garcia-Rincon, D., de la Prida, L.M., and Ascoli, G.A. (2021).
1138 An update to Hippocampome.org by integrating single-cell phenotypes with circuit function
1139 in vivo. PLoS Biol *19*, e3001213. 10.1371/journal.pbio.3001213.
1140 20. Nishimura, M., Tomimoto, H., Suenaga, T., Namba, Y., Ikeda, K., Akiguchi, I., and Kimura, J.
1141 (1995). Immunocytochemical characterization of glial fibrillary tangles in Alzheimer's disease
1142 brain. Am J Pathol *146*, 1052-1058.
1143 21. Arima, K. (1996). Tubular profile of the Gallyas- and tau-positive argyrophilic threads in
1144 corticobasal degeneration: An electronmicroscopic study. Neuropathology *16*, 65-70.
1145 10.1111/j.1440-1789.1996.tb00157.x.
1146 22. Arima, K., Nakamura, M., Sunohara, N., Ogawa, M., Anno, M., Izumiyama, Y., Hirai, S., and
1147 Ikeda, K. (1997). Ultrastructural characterization of the tau-immunoreactive tubules in the
1148 oligodendroglial perikarya and their inner loop processes in progressive supranuclear palsy.
1149 Acta Neuropathol *93*, 558-566. 10.1007/s004010050652.
1150 23. Peters, A., and Sethares, C. (2004). Oligodendrocytes, their progenitors and other neuroglial
1151 cells in the aging primate cerebral cortex. Cereb Cortex *14*, 995-1007.
1152 10.1093/cercor/bhh060.
1153 24. Lin, W.L., Lewis, J., Yen, S.H., Hutton, M., and Dickson, D.W. (2003). Filamentous tau in
1154 oligodendrocytes and astrocytes of transgenic mice expressing the human tau isoform with
1155 the P301L mutation. Am J Pathol *162*, 213-218. 10.1016/S0002-9440(10)63812-6.
1156 25. Caroni, P. (1997). Overexpression of growth-associated proteins in the neurons of adult
1157 transgenic mice. J Neurosci Methods *71*, 3-9. 10.1016/s0165-0270(96)00121-5.
1158 26. Bannerman, D.M., Niewoehner, B., Lyon, L., Romberg, C., Schmitt, W.B., Taylor, A.,
1159 Sanderson, D.J., Cottam, J., Sprengel, R., Seeburg, P.H., et al. (2008). NMDA receptor subunit
1160 NR2A is required for rapidly acquired spatial working memory but not incremental spatial
1161 reference memory. J Neurosci *28*, 3623-3630. 10.1523/JNEUROSCI.3639-07.2008.
1162 27. Belarbi, K., Burnouf, S., Fernandez-Gomez, F.J., Desmercieres, J., Troquier, L., Brouillette, J.,
1163 Tsambou, L., Grosjean, M.E., Caillierez, R., Demeyer, D., et al. (2011). Loss of medial septum
1164 cholinergic neurons in THY-Tau22 mouse model: what links with tau pathology? Curr
1165 Alzheimer Res *8*, 633-638. 10.2174/156720511796717230.
1166 28. Van der Jeugd, A., Ahmed, T., Burnouf, S., Belarbi, K., Hamdame, M., Grosjean, M.E., Humez,
1167 S., Balschun, D., Blum, D., Buee, L., and D'Hooge, R. (2011). Hippocampal tauopathy in tau
1168 transgenic mice coincides with impaired hippocampus-dependent learning and memory, and
1169 attenuated late-phase long-term depression of synaptic transmission. Neurobiol Learn Mem
1170 *95*, 296-304. 10.1016/j.nlm.2010.12.005.
1171 29. Sri, S., Pegasiou, C.M., Cave, C.A., Hough, K., Wood, N., Gomez-Nicola, D., Deinhardt, K.,
1172 Bannerman, D., Perry, V.H., and Vargas-Caballero, M. (2019). Emergence of synaptic and

cognitive impairment in a mature-onset APP mouse model of Alzheimer's disease. Acta Neuropathol Commun *7*, 25. 10.1186/s40478-019-0670-1.

30. Pritchett, D., Taylor, A.M., Barkus, C., Engle, S.J., Brandon, N.J., Sharp, T., Foster, R.G., Harrison, P.J., Peirson, S.N., and Bannerman, D.M. (2016). Searching for cognitive enhancement in the Morris water maze: better and worse performance in D-amino acid oxidase knockout (Dao(-/-)) mice. Eur J Neurosci *43*, 979-989. 10.1111/ejn.13192.

31. Lyon, L., Burnet, P.W., Kew, J.N., Corti, C., Rawlins, J.N., Lane, T., De Filippis, B., Harrison, P.J., and Bannerman, D.M. (2011). Fractionation of spatial memory in GRM2/3 (mGlu2/mGlu3) double knockout mice reveals a role for group II metabotropic glutamate receptors at the interface between arousal and cognition. Neuropsychopharmacology *36*, 2616-2628. 10.1038/npp.2011.145.

32. Reisel, D., Bannerman, D.M., Schmitt, W.B., Deacon, R.M., Flint, J., Borchardt, T., Seeburg, P.H., and Rawlins, J.N. (2002). Spatial memory dissociations in mice lacking GluR1. Nat Neurosci *5*, 868-873. 10.1038/nn910.

33. Kjelstrup, K.G., Tuvnes, F.A., Steffenach, H.A., Murison, R., Moser, E.I., and Moser, M.B. (2002). Reduced fear expression after lesions of the ventral hippocampus. Proc Natl Acad Sci U S A *99*, 10825-10830. 10.1073/pnas.152112399.

34. Bannerman, D.M., Rawlins, J.N., McHugh, S.B., Deacon, R.M., Yee, B.K., Bast, T., Zhang, W.N., Pothuizen, H.H., and Feldon, J. (2004). Regional dissociations within the hippocampus--memory and anxiety. Neurosci Biobehav Rev *28*, 273-283. 10.1016/j.neubiorev.2004.03.004.

35. Ahnaou, A., Moechars, D., Raeymaekers, L., Biermans, R., Manyakov, N.V., Bottelbergs, A., Wintmolders, C., Van Kolen, K., Van De Casteele, T., Kemp, J.A., and Drinkenburg, W.H. (2017). Emergence of early alterations in network oscillations and functional connectivity in a tau seeding mouse model of Alzheimer's disease pathology. Sci Rep *7*, 14189. 10.1038/s41598-017-13839-6.

36. Wang, Y., Romani, S., Lustig, B., Leonardo, A., and Pastalkova, E. (2015). Theta sequences are essential for internally generated hippocampal firing fields. Nat Neurosci *18*, 282-288. 10.1038/nn.3904.

37. Menkes-Caspi, N., Yamin, H.G., Kellner, V., Spires-Jones, T.L., Cohen, D., and Stern, E.A. (2015). Pathological tau disrupts ongoing network activity. Neuron *85*, 959-966. 10.1016/j.neuron.2015.01.025.

38. Csicsvari, J., Hirase, H., Czurko, A., Mamiya, A., and Buzsaki, G. (1999). Oscillatory coupling of hippocampal pyramidal cells and interneurons in the behaving Rat. J Neurosci *19*, 274-287.

39. Lopes-Dos-Santos, V., van de Ven, G.M., Morley, A., Trouche, S., Campo-Urriza, N., and Dupret, D. (2018). Parsing Hippocampal Theta Oscillations by Nested Spectral Components during Spatial Exploration and Memory-Guided Behavior. Neuron *100*, 940-952 e947. 10.1016/j.neuron.2018.09.031.

40. Quinn, A.J., Lopes-Dos-Santos, V., Huang, N., Liang, W.K., Juan, C.H., Yeh, J.R., Nobre, A.C., Dupret, D., and Woolrich, M.W. (2021). Within-cycle instantaneous frequency profiles report oscillatory waveform dynamics. J Neurophysiol *126*, 1190-1208. 10.1152/jn.00201.2021.

41. Canolty, R.T., Edwards, E., Dalal, S.S., Soltani, M., Nagarajan, S.S., Kirsch, H.E., Berger, M.S., Barbaro, N.M., and Knight, R.T. (2006). High gamma power is phase-locked to theta oscillations in human neocortex. Science *313*, 1626-1628. 10.1126/science.1128115.

42. Goodman, M.S., Kumar, S., Zomorrodi, R., Ghazala, Z., Cheam, A.S.M., Barr, M.S., Daskalakis, Z.J., Blumberger, D.M., Fischer, C., Flint, A., et al. (2018). Theta-Gamma Coupling and Working Memory in Alzheimer's Dementia and Mild Cognitive Impairment. Front Aging Neurosci *10*, 101. 10.3389/fnagi.2018.00101.

43. Lasztoczi, B., and Klausberger, T. (2017). Distinct gamma oscillations in the distal dendritic fields of the dentate gyrus and the CA1 area of mouse hippocampus. Brain Struct Funct *222*, 3355-3365. 10.1007/s00429-017-1421-3.

44. Buzsaki, G. (2015). Hippocampal sharp wave-ripple: A cognitive biomarker for episodic memory and planning. Hippocampus *25*, 1073-1188. 10.1002/hipo.22488.
45. Mizuseki, K., and Buzsaki, G. (2013). Preconfigured, skewed distribution of firing rates in the hippocampus and entorhinal cortex. Cell Rep *4*, 1010-1021. 10.1016/j.celrep.2013.07.039.
46. Skaggs, W.E., McNaughton, B.L., Wilson, M.A., and Barnes, C.A. (1996). Theta phase precession in hippocampal neuronal populations and the compression of temporal sequences. Hippocampus *6*, 149-172. 10.1002/(SICI)1098-1063(1996)6:2<149::AID-HIPO6>3.0.CO;2-K.
47. Chen, G., King, J.A., Burgess, N., and O'Keefe, J. (2013). How vision and movement combine in the hippocampal place code. Proc Natl Acad Sci U S A *110*, 378-383. 10.1073/pnas.1215834110.
48. Ising, C., Venegas, C., Zhang, S., Scheiblich, H., Schmidt, S.V., Vieira-Saecker, A., Schwartz, S., Albasset, S., McManus, R.M., Tejera, D., et al. (2019). NLRP3 inflammasome activation drives tau pathology. Nature *575*, 669-673. 10.1038/s41586-019-1769-z.
49. Gotz, J., Chen, F., Barmettler, R., and Nitsch, R.M. (2001). Tau filament formation in transgenic mice expressing P301L tau. J Biol Chem *276*, 529-534. 10.1074/jbc.M006531200.
50. Grueninger, F., Bohrmann, B., Czech, C., Ballard, T.M., Frey, J.R., Weidensteiner, C., von Kienlin, M., and Ozmen, L. (2010). Phosphorylation of Tau at S422 is enhanced by Abeta in TauPS2APP triple transgenic mice. Neurobiol Dis *37*, 294-306. 10.1016/j.nbd.2009.09.004.
51. Probst, A., Gotz, J., Wiederhold, K.H., Tolnay, M., Mistl, C., Jaton, A.L., Hong, M., Ishihara, T., Lee, V.M., Trojanowski, J.Q., et al. (2000). Axonopathy and amyotrophy in mice transgenic for human four-repeat tau protein. Acta Neuropathol *99*, 469-481. 10.1007/s004010051148.
52. Ferrer, I. (2018). Oligodendrogliopathy in neurodegenerative diseases with abnormal protein aggregates: The forgotten partner. Prog Neurobiol *169*, 24-54. 10.1016/j.pneurobio.2018.07.004.
53. Shi, Y., Zhang, W., Yang, Y., Murzin, A.G., Falcon, B., Kotecha, A., van Beers, M., Tarutani, A., Kametani, F., Garringer, H.J., et al. (2021). Structure-based classification of tauopathies. Nature *598*, 359-363. 10.1038/s41586-021-03911-7.
54. Ferrer, I., Aguilo Garcia, M., Carmona, M., Andres-Benito, P., Torrejon-Escribano, B., Garcia-Esparcia, P., and Del Rio, J.A. (2019). Involvement of Oligodendrocytes in Tau Seeding and Spreading in Tauopathies. Front Aging Neurosci *11*, 112. 10.3389/fnagi.2019.00112.
55. Clavaguera, F., Akatsu, H., Fraser, G., Crowther, R.A., Frank, S., Hench, J., Probst, A., Winkler, D.T., Reichwald, J., Staufenbiel, M., et al. (2013). Brain homogenates from human tauopathies induce tau inclusions in mouse brain. Proc Natl Acad Sci U S A *110*, 9535-9540. 10.1073/pnas.1301175110.
56. Clavaguera, F., Bolmont, T., Crowther, R.A., Abramowski, D., Frank, S., Probst, A., Fraser, G., Stalder, A.K., Beibel, M., Staufenbiel, M., et al. (2009). Transmission and spreading of tauopathy in transgenic mouse brain. Nat Cell Biol *11*, 909-913. 10.1038/ncb1901.
57. Poliak, S., and Peles, E. (2003). The local differentiation of myelinated axons at nodes of Ranvier. Nat Rev Neurosci *4*, 968-980. 10.1038/nrn1253.
58. Ikeda, K., Akiyama, H., Haga, C., Kondo, H., Arima, K., and Oda, T. (1994). Argyrophilic thread-like structure in corticobasal degeneration and supranuclear palsy. Neurosci Lett *174*, 157-159. 10.1016/0304-3940(94)90010-8.
59. Ferreira, S., Pitman, K.A., Summers, B.S., Wang, S., Young, K.M., and Cullen, C.L. (2021). Oligodendrogenesis increases in hippocampal grey and white matter prior to locomotor or memory impairment in an adult mouse model of tauopathy. Eur J Neurosci *54*, 5762-5784. 10.1111/ejn.14726.
60. Steadman, P.E., Xia, F., Ahmed, M., Mocle, A.J., Penning, A.R.A., Geraghty, A.C., Steenland, H.W., Monje, M., Josselyn, S.A., and Frankland, P.W. (2020). Disruption of Oligodendrogenesis Impairs Memory Consolidation in Adult Mice. Neuron *105*, 150-164 e156. 10.1016/j.neuron.2019.10.013.

1274 61. Iram, T., Kern, F., Kaur, A., Myneni, S., Morningstar, A.R., Shin, H., Garcia, M.A., Yerra, L.,
1275 Palovics, R., Yang, A.C., et al. (2022). Young CSF restores oligodendrogenesis and memory in
1276 aged mice via Fgf17. Nature *605*, 509-515. 10.1038/s41586-022-04722-0.
1277 62. Battefeld, A., Klooster, J., and Kole, M.H. (2016). Myelinating satellite oligodendrocytes are
1278 integrated in a glial syncytium constraining neuronal high-frequency activity. Nat Commun *7*,
1279 11298. 10.1038/ncomms11298.
1280 63. Salib, M., Joshi, A., Katona, L., Howarth, M., Micklem, B.R., Somogyi, P., and Viney, T.J.
1281 (2019). GABAergic Medial Septal Neurons with Low-Rhythmic Firing Innervating the Dentate
1282 Gyrus and Hippocampal Area CA3. J Neurosci *39*, 4527-4549. 10.1523/JNEUROSCI.3024-
1283 18.2019.
1284 64. Viney, T.J., Salib, M., Joshi, A., Unal, G., Berry, N., and Somogyi, P. (2018). Shared rhythmic
1285 subcortical GABAergic input to the entorhinal cortex and presubiculum. Elife *7*.
1286 10.7554/eLife.34395.
1287 65. Joshi, A., Salib, M., Viney, T.J., Dupret, D., and Somogyi, P. (2017). Behavior-Dependent
1288 Activity and Synaptic Organization of Septo-hippocampal GABAergic Neurons Selectively
1289 Targeting the Hippocampal CA3 Area. Neuron *96*, 1342-1357 e1345.
1290 10.1016/j.neuron.2017.10.033.
1291 66. Jeffery, K.J., Donnett, J.G., and O'Keefe, J. (1995). Medial septal control of theta-correlated
1292 unit firing in the entorhinal cortex of awake rats. Neuroreport *6*, 2166-2170.
1293 10.1097/00001756-199511000-00017.
1294 67. Wang, X.J. (2002). Pacemaker neurons for the theta rhythm and their synchronization in the
1295 septohippocampal reciprocal loop. J Neurophysiol *87*, 889-900. 10.1152/jn.00135.2001.
1296 68. Leutgeb, S., and Mizumori, S.J. (1999). Excitotoxic septal lesions result in spatial memory
1297 deficits and altered flexibility of hippocampal single-unit representations. J Neurosci *19*,
1298 6661-6672.
1299 69. Buzsaki, G., Leung, L.W., and Vanderwolf, C.H. (1983). Cellular bases of hippocampal EEG in
1300 the behaving rat. Brain Res *287*, 139-171. 10.1016/0165-0173(83)90037-1.
1301 70. Wu, D., Gao, D., Yu, H., Pi, G., Xiong, R., Lei, H., Wang, X., Liu, E., Ye, J., Yu, H., et al. (2021).
1302 Medial septum tau accumulation induces spatial memory deficit via disrupting medial
1303 septum-hippocampus cholinergic pathway. Clin Transl Med *11*, e428. 10.1002/ctm2.428.
1304 71. Viena, T.D., Linley, S.B., and Vertes, R.P. (2018). Inactivation of nucleus reuniens impairs
1305 spatial working memory and behavioral flexibility in the rat. Hippocampus *28*, 297-311.
1306 10.1002/hipo.22831.
1307 72. Frost, B.E., Martin, S.K., Cafalchio, M., Islam, M.N., Aggleton, J.P., and O'Mara, S.M. (2021).
1308 Anterior Thalamic Inputs Are Required for Subiculum Spatial Coding, with Associated
1309 Consequences for Hippocampal Spatial Memory. J Neurosci *41*, 6511-6525.
1310 10.1523/JNEUROSCI.2868-20.2021.
1311 73. Berardi, N., Braschi, C., Capsoni, S., Cattaneo, A., and Maffei, L. (2007). Environmental
1312 enrichment delays the onset of memory deficits and reduces neuropathological hallmarks in
1313 a mouse model of Alzheimer-like neurodegeneration. J Alzheimers Dis *11*, 359-370.
1314 10.3233/jad-2007-11312.
1315 74. Sanderson, D.J., Good, M.A., Skelton, K., Sprengel, R., Seeburg, P.H., Rawlins, J.N., and
1316 Bannerman, D.M. (2009). Enhanced long-term and impaired short-term spatial memory in
1317 GluA1 AMPA receptor subunit knockout mice: evidence for a dual-process memory model.
1318 Learn Mem *16*, 379-386. 10.1101/lm.1339109.
1319 75. Sanderson, D.J., Gray, A., Simon, A., Taylor, A.M., Deacon, R.M., Seeburg, P.H., Sprengel, R.,
1320 Good, M.A., Rawlins, J.N., and Bannerman, D.M. (2007). Deletion of glutamate receptor-A
1321 (GluR-A) AMPA receptor subunits impairs one-trial spatial memory. Behav Neurosci *121*,
1322 559-569. 10.1037/0735-7044.121.3.559.

76. Lever, C., Burton, S., Jeewajee, A., O'Keefe, J., and Burgess, N. (2009). Boundary vector cells in the subiculum of the hippocampal formation. J Neurosci *29*, 9771-9777. 10.1523/JNEUROSCI.1319-09.2009.
77. Bannerman, D.M., Grubb, M., Deacon, R.M.J., Yee, B.K., Feldon, J., and Rawlins, J.N.P. (2003). Ventral hippocampal lesions affect anxiety but not spatial learning. Behavioural Brain Research *139*, 197-213. 10.1016/s0166-4328(02)00268-1.
78. Trivedi, M.A., and Coover, G.D. (2004). Lesions of the ventral hippocampus, but not the dorsal hippocampus, impair conditioned fear expression and inhibitory avoidance on the elevated T-maze. Neurobiol Learn Mem *81*, 172-184. 10.1016/j.nlm.2004.02.005.
79. Busche, M.A., Wegmann, S., Dujardin, S., Commins, C., Schiantarelli, J., Klickstein, N., Kamath, T.V., Carlson, G.A., Nelken, I., and Hyman, B.T. (2019). Tau impairs neural circuits, dominating amyloid-beta effects, in Alzheimer models in vivo. Nat Neurosci *22*, 57-64. 10.1038/s41593-018-0289-8.
80. Mably, A.J., Gereke, B.J., Jones, D.T., and Colgin, L.L. (2017). Impairments in spatial representations and rhythmic coordination of place cells in the 3xTg mouse model of Alzheimer's disease. Hippocampus *27*, 378-392. 10.1002/hipo.22697.
81. Buzsáki, G. (2019). The Brain from Inside Out (Oxford University Press). 10.1093/oso/9780190905385.001.0001.
82. Booth, C.A., Ridler, T., Murray, T.K., Ward, M.A., de Groot, E., Goodfellow, M., Phillips, K.G., Randall, A.D., and Brown, J.T. (2016). Electrical and Network Neuronal Properties Are Preferentially Disrupted in Dorsal, But Not Ventral, Medial Entorhinal Cortex in a Mouse Model of Tauopathy. J Neurosci *36*, 312-324. 10.1523/JNEUROSCI.2845-14.2016.
83. Long, S., Wu, Z., and Huang, N. (2008). Hilbert-Huang transform. Scholarpedia *3*, 2544. 10.4249/scholarpedia.2544.
84. Stringer, C., Pachitariu, M., Steinmetz, N., Reddy, C.B., Carandini, M., and Harris, K.D. (2019). Spontaneous behaviors drive multidimensional, brainwide activity. Science *364*, 255. 10.1126/science.aav7893.
85. Rossant, C., Kadir, S.N., Goodman, D.F.M., Schulman, J., Hunter, M.L.D., Saleem, A.B., Grosmark, A., Belluscio, M., Denfield, G.H., Ecker, A.S., et al. (2016). Spike sorting for large, dense electrode arrays. Nat Neurosci *19*, 634-641. 10.1038/nn.4268.
86. Ozdemir, A.T., Lagler, M., Lagoun, S., Malagon-Vina, H., Lasztoczi, B., and Klausberger, T. (2020). Unexpected Rule-Changes in a Working Memory Task Shape the Firing of Histologically Identified Delay-Tuned Neurons in the Prefrontal Cortex. Cell Rep *30*, 1613-1626 e1614. 10.1016/j.celrep.2019.12.102.
87. Pennington, Z.T., Dong, Z., Feng, Y., Vetere, L.M., Page-Harley, L., Shuman, T., and Cai, D.J. (2019). ezTrack: An open-source video analysis pipeline for the investigation of animal behavior. Sci Rep *9*, 19979. 10.1038/s41598-019-56408-9.
88. Goedert, M., Jakes, R., and Vanmechelen, E. (1995). Monoclonal antibody AT8 recognises tau protein phosphorylated at both serine 202 and threonine 205. Neurosci Lett *189*, 167-169. 10.1016/0304-3940(95)11484-e.
89. Viney, T.J., Lasztoczi, B., Katona, L., Crump, M.G., Tukker, J.J., Klausberger, T., and Somogyi, P. (2013). Network state-dependent inhibition of identified hippocampal CA3 axo-axonic cells in vivo. Nat Neurosci *16*, 1802-1811. 10.1038/nn.3550.
90. Unal, G., Joshi, A., Viney, T.J., Kis, V., and Somogyi, P. (2015). Synaptic Targets of Medial Septal Projections in the Hippocampus and Extrahippocampal Cortices of the Mouse. J Neurosci *35*, 15812-15826. 10.1523/JNEUROSCI.2639-15.2015.